

Measurement and evaluation of the crystallization kinetics of L-asparagine monohydrate in the ternary L-/ D-asparagine/ water system

Erik Temmel^{a*}, Jonathan Gänsch^a, Heike Lorenz^a, Andreas Seidel-Morgenstern^{a,b}

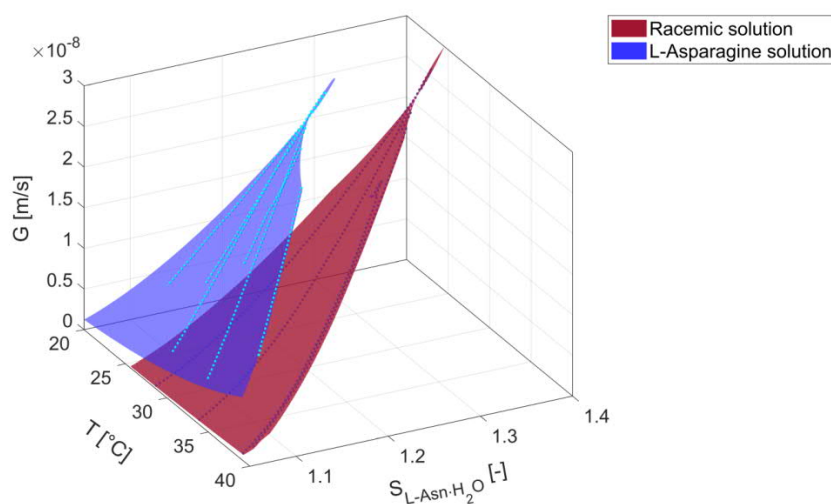
^aMax Planck Institute for Dynamics of Complex Technical Systems, Sandtorstraße 1, 39106 Magdeburg, Germany

^bOtto von Guericke University Magdeburg, Chair of Chemical Process Engineering, 39106 Magdeburg, Germany

Abstract

Growth kinetics of L-asparagine monohydrate in racemic aqueous solutions as well as nucleation, growth and dissolution kinetics of the same enantiomer crystallized from pure L-asparagine solutions are measured and the kinetic parameters are estimated applying a recently developed shortcut-method. The corresponding experimental procedure is based on a small number of preferential (seeded) cooling crystallizations where the crystal size distribution is monitored with an online microscope. Afterwards, image analysis yields the transient particle size evolution of initially provided crystals, from which the response of the solid phase to the liquid phase driving force can be extracted. Subsequently, parameter estimation is carried out applying this data together with the information of concentration and composition of the liquid phase, to discriminate between different model approaches. The kinetics are validated finally with independent experiments to evaluate their quality.

It is proven that growth kinetics of L- and D-asparagine monohydrate from water are identical. In contrast, it can be shown and quantified, that growth kinetics from racemic and enantiopure solutions of asparagine differ significantly from each other. The corresponding calculation of the driving force of enantiomeric systems is discussed in detail by means of ternary phase diagrams.



Corresponding author: Andreas Seidel-Morgenstern
Max Planck Institute for Dynamics of Complex Technical
Systems; Sandtorstraße 1, 39106 Magdeburg, Germany
Tel: +49 391 6110401; Fax: +49 391 6110521
Email: seidel@mpi-magdeburg.mpg.de

Measurement and evaluation of the crystallization kinetics of L-asparagine monohydrate in the ternary L-/ D-asparagine/ water system

Erik Temmel^a, Jonathan Gänsch^a, Heike Lorenz^a, Andreas Seidel-Morgenstern^{a,b,*}

^aMax Planck Institute for Dynamics of Complex Technical Systems, Sandtorstraße 1, 39106

Magdeburg, Germany

^bOtto von Guericke University Magdeburg, Chair of Chemical Process Engineering, 39106

Magdeburg, Germany

*Corresponding author, seidel@ mpi-magdeburg.mpg.de

Abstract

Growth kinetics of L-asparagine monohydrate in racemic aqueous solutions as well as nucleation, growth and dissolution kinetics of the same enantiomer crystallized from pure L-asparagine solutions are measured and the kinetic parameters are estimated applying a recently developed shortcut-method. The corresponding experimental procedure is based on a small number of preferential (seeded) cooling crystallizations where the crystal size distribution is monitored with an online microscope. Afterwards, image analysis yields the transient particle size evolution of initially provided crystals, from which the response of the solid phase to the liquid phase driving force can be extracted. Subsequently, parameter estimation is carried out applying this data together with the information of concentration and composition of the liquid phase, to discriminate between different model approaches. The kinetics are validated finally with independent experiments to evaluate their quality.

It is proven that growth kinetics of L- and D-asparagine monohydrate from water are identical. In contrast, it can be shown and quantified, that growth kinetics from racemic and enantiopure

solutions of asparagine differ significantly from each other. The corresponding calculation of the driving force of enantiomeric systems is discussed in detail by means of ternary phase diagrams.

Keywords: Enantioseparation, Crystallization kinetics, Ternary phase equilibria, Admixture effects, Asparagine, Population balance equations

1. Introduction

Population balance equations (PBE) present a sophisticated and well-studied mathematical basis to describe and optimize crystallization based-processes. The general equations were developed during the past decades and have been studied intensively since then [1, 2]. New applications of this model framework are continuously developed in various fields, e.g. for the description of crystallization-based enantioseparation processes like Viedma Ripening or Preferential Crystallization [3-10].

Preferential Crystallization (PC), for example, requires that growth kinetics are fast enough to yield a sufficient depletion of the crystallizing enantiomer in the liquid phase, i.e. a sufficient “entrainment”, before the dissolved antipode nucleates. Hence, crystallization kinetics play an important role for this elegant but fragile resolution method similarly to other sophisticated solidification processes [11-13] and PBE modeling can be beneficial to identify suitable initial and operating conditions.

A recently developed shortcut method [14, 15] will be applied in this study to estimate crystallization kinetics that are necessary to link the mathematical framework to the process type and the chiral substance system of interest. This method is based on measuring the liquid and solid phase evolution of a few polythermal preferential batch crystallizations. The state of the

solution, defined by composition and temperature, is subsequently utilized to calculate the crystallization driving force for each enantiomer. Changes in the crystal size distribution (CSD) and number of crystals are tracked by an image-based online measurement technique. The recorded images are automatically evaluated afterwards with respect to the dimensions of the observed single crystals. From this extracted single crystal size distribution (Fig. 1), only the initially present seed material is of interest for growth and dissolution.

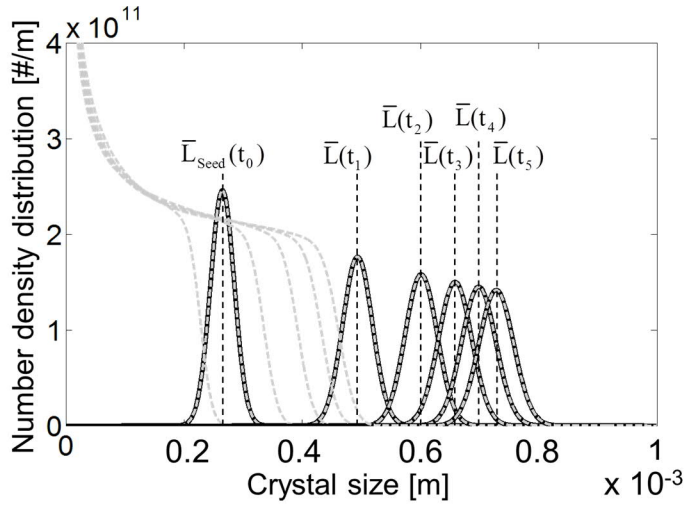


Fig. 1: Simulated solid phase evolution of a generic substance system. Each crystal size distribution (CSD, grey dashed lines) depicts one measured sample at different time instances (t_0 - t_5). Black lines depict the evolution of the initially present seed material and black dashed lines the calculated mean size of the grown seed fraction.

Assuming that the crystallizer is well-mixed and crystals evolve size-independently, growth and dissolution rates should be the same for each individual of the whole population. Hence, it is straightforward to look for the transient of the mean size of the seed fraction (black lines in Fig. 1) to have an objective measure on the impact of the growth (G) and dissolution (D) kinetics on

the total population [16]. This mean size evolution can then be used, together with the driving force of the corresponding enantiomer, to estimate directly the kinetic parameters of a corresponding mathematical approach without the usage of a full PBE model. A similar procedure is followed to estimate nucleation kinetics (B_0) from the crystal number evolution.

In the following, the experimental setup, the substance system and the general procedure of the shortcut method are explained in detail, followed by a discussion on the calculation of the driving force for chiral systems. This shortcut method will then be applied to asparagine monohydrate, a non-essential amino acid, which is also the focus of a few recent publications [17-20] to determine growth, nucleation and dissolution kinetics. There is evidence, that the presence of the counter enantiomer influences crystallization kinetics of L·Asn [19, 20]. Hence, this study aims to clarify this effect over a broader range of operating conditions (i.e. temperature and supersaturation).

2. Experiments

2.1. Substances and characteristics of the asparagine monohydrate/ water model system

For the crystallization experiments, racemic Asparagine monohydrate and L-Asparagine monohydrate were purchased from Sigma Aldrich (Purity >99 %). Both were used without further treatment. D-asparagine monohydrate was crystallized from D-Asn enriched mother liquors obtained from Preferential Crystallizations with L-Asn (see Table 2 and section 3.2). Perchloric acid, which served as eluent for HPLC analysis was ordered from Merck (Purity 70-72 %). Deionized water (Millipore, Milli-Q Advantage A10) was used for analysis, washing of

the crystalline product and the actual experiments. Ethanol, used for the washing procedure as well, was purchased from VWR Chemicals (Purity >99.7%).

L-/ D-asparagine monohydrate is a conglomerate forming system [21] and therefore Preferential Crystallization (PC) can be applied directly from a supersaturated racemic liquid phase. Relevant physical properties are listed in table 1. The specified volume shape factor was calculated from the average of length and width from the measured crystals of all experiments assuming a rectangular prism shape. The volume shape factor relates the volume of a crystal to the volume of a perfect cube with respect to the same characteristic length [1], which is in case of asparagine monohydrate the crystal width, and is necessary for utilizing of population balance models. The factor was almost constant during the experiments and a dependence of the morphology of the asparagine monohydrate crystals on the operation conditions was not observed.

Table 1: Relevant physical properties of asparagine monohydrate (racemic Asn·H₂O is only a physical mixture of D- and L-asparagine monohydrate).

Property	Unit	Value
Molar mass (monohydrate), $M_{\text{hydr.}}$	g/mol	150.13
Molar mass (anhydrous), $M_{\text{anhydr.}}$	g/mol	132.12
Solid density, ρ_s	g/cm ³	1.54
Volume shape factor, k_v	-	1.85

Solubility data of L-Asn·H₂O was taken from [21] (black dots in Fig. 2) and mirrored to the D-Asn·H₂O assuming identical solubilities of both enantiomers. The data was verified by additional isothermal solubility measurements (white dots in Fig. 2). The corresponding ternary phase

diagram forms the basis of the experimental design and supersaturation calculation, which is explained in section 3.1.

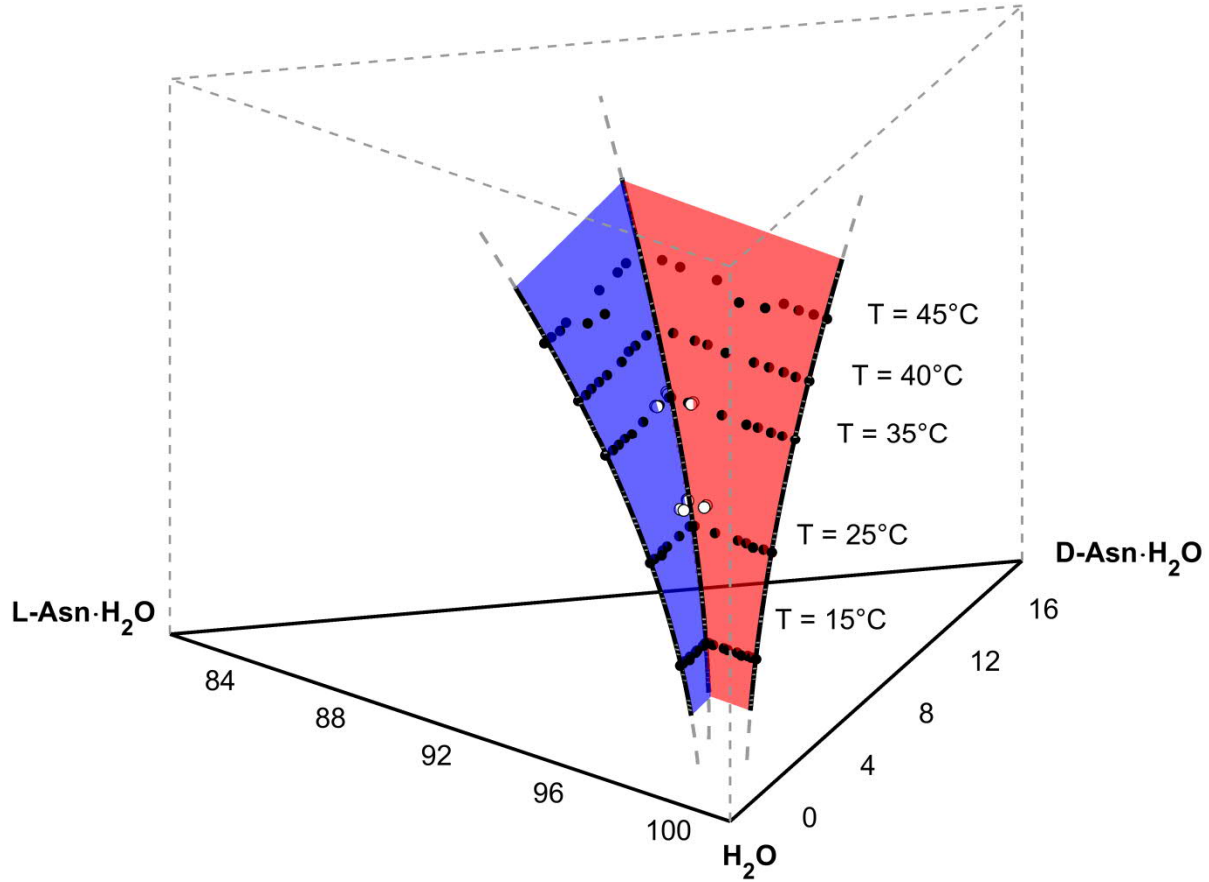


Fig. 2: Relevant part of the ternary phase diagram (20% section of the entire diagram) of the asparagine monohydrate enantiomers in water at different indicated temperatures [22]. Axes are given in mass fractions $x_i \cdot 100$ (wt%). Black dots - solubility data from [21]; White dots - newly measured solubilities; Red surface - fitted solubility surface of D-Asn-H₂O; Blue surface - fitted solubility surface of L-Asn-H₂O.

2.2. Experimental setup

All polythermal crystallization experiments were carried out in a 2.5L double-walled crystallizer equipped with a baffled draft tube (Fig. 3). Temperature was monitored by a Pt 100 and a corresponding instrument transformer (Ahlborn Mess- und Regelungstechnik, Almemo 2590-4S, accuracy: $\pm 0.1\text{K}$). A calibrated densitometer (Mettler Toledo, Densitometer DE40) fed by a peristaltic pump (Heidolph, Pumpdrive 5201, $\dot{V} = 35.6 \text{ ml/min}$) served to measure the total asparagine concentration of the solid-free liquid phase. Additional crystal-free offline samples were withdrawn every 6-7 minutes to investigate the enantiomeric composition via HPLC analysis.

A commercially available online microscope (QicPic, Sympatec) was utilized to record the solid phase evolution. Therefore, the suspension was withdrawn unclassified by a peristaltic pump (Ismatec, ISM915A, $\dot{V} = 540 \text{ ml/min}$) and pumped through a cuvette located inside the system. A light source and camera were attached on opposite sides of the cuvette, perpendicular to the flow path. Up to 25 greyscale images per second can be recorded of the bypassing suspension. This image data is subsequently analyzed automatically [23, 24] with respect to the dimensions of the recorded single crystals. In addition, sieve and phase analyses of the solid products were performed as described below.

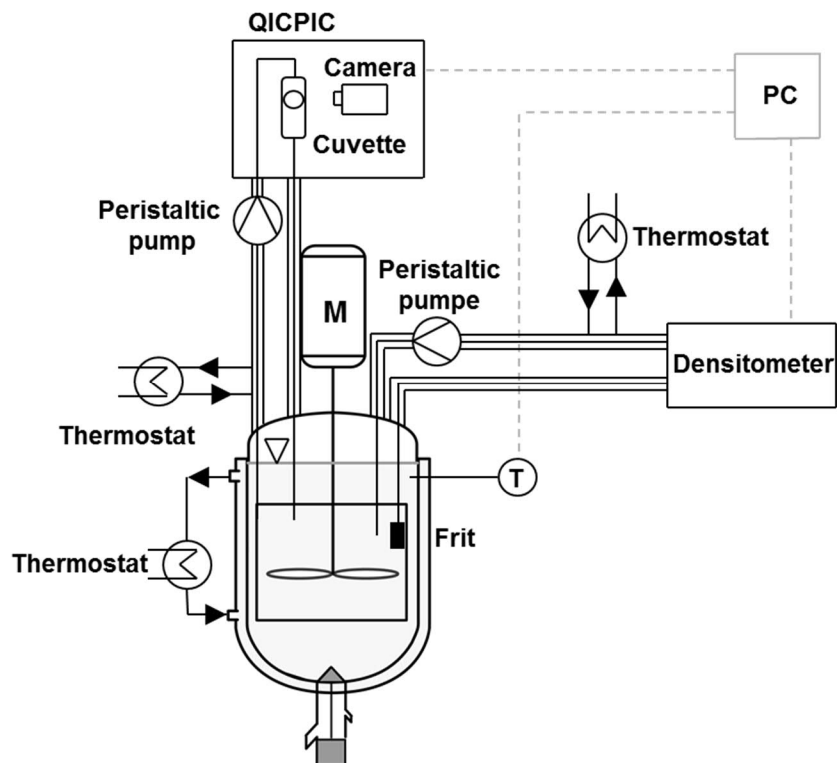


Fig. 3: Utilized 2.5L DTB double-wall crystallizer equipped with an online microscope (QicPic, Sympatec), a temperature sensor (T) and a densitometer (Mettler Toledo, DE40). All tubes were heated by thermostats (Lauda, RPC 845) to prevent blocking or encrustation.

2.3. HPLC analysis

Offline samples of the liquid phase and the solid products of each experiment used for growth kinetics estimation in racemic solution as well as each fraction of the sieved products were investigated by HPLC with respect to purity and composition. A Crownpak CR(+) (4x150 mm, particle size 5 μm) column was utilized with a Dionex Ultimate 3000 system (Thermo Scientific) and perchloric acid/ water (pH = 1) as the eluent. The flow rate, UV wave length, column temperature and injection volume were 0.4 ml/min, 200 nm, 5°C and 1 μl , respectively.

2.4. Sieve analysis

Sieve analyses (Retsch, AS 200 digit) of every product were performed to confirm and complement the measurements of the online microscope. Each product sieve fraction (sieve fraction were 90 μm - 1 mm) from the PC experiments (for growth kinetic estimation in racemic solution) was additionally investigated with respect to purity to evaluate the contamination of the preferred enantiomer with its antipode due to primary nucleation.

2.5. X-Ray Powder Diffraction phase analysis

The solid products were investigated on an X'Pert Pro diffractometer (PANalytical GmbH, Germany) in a 2-theta range of 5-40° with a step size and step time of 0.017° and 50s, respectively. No phase change was observed during the investigations and always the monohydrate of asparagine was crystallized.

2.6. Experimental procedure

Three sets of experiments were planned to investigate and evaluate the crystallization kinetics under different conditions. The first set (referred to as DL#) was started from clear saturated racemic solutions. The second set (referred to as L#) was carried out in enantiopure L-Asn solutions. Two experiments of the last set of validation experiments, which were not utilized for parameter estimation, were started from racemic liquid phase composition (referred to as Val-DL#) and one experiment again from L-Asn solution (referred to as Val-L#). All experiments are listed in table 2.

Clear saturated solutions (DL-Asn or L-Asn solutions, Table 2) for each experiment were prepared based on the solubility data shown in Fig. 2 for the respective saturation temperature

(T_{sat} , Table 2). Saturation temperatures were chosen to investigate the kinetics in the range of the known part of the ternary phase diagram. Saturation temperatures $>40^{\circ}\text{C}$ were neglected due to the high probability of crystallization inside the online microscope bypass.

Table 2: List of all experiments carried out for this study with the corresponding conditions. T_{sat} - saturation temperature; $m_{\text{sat, DL-/L-Asn}\cdot\text{H}_2\text{O}}$ - mass of racemic or L-asparagine monohydrate for saturation; $m_{\text{H}_2\text{O}}$ - mass of initially provided water; $\Delta T/\Delta t$ - linear cooling (-) or heating rate (+).

Exp.	T_{sat} [$^{\circ}\text{C}$]	$m_{\text{sat,DL-/L-Asn}\cdot\text{H}_2\text{O}}$ [kg]	$m_{\text{H}_2\text{O}}$ [kg]	$\Delta T/\Delta t$ [K/h]	Seeded enantiomer and fraction [μm]
DL1	40	294	2300	-3	L-Asn \cdot H ₂ O, 90-125
DL2	40	294	2300	-5	L-Asn \cdot H ₂ O, 90-125
DL3	35	231	2300	-5	L-Asn \cdot H ₂ O, 90-125
DL4	30	188	2400	-5	L-Asn \cdot H ₂ O, 90-125
L1	40	146	2500	-5 / +20	L-Asn \cdot H ₂ O, 90-125
L2	35	118	2500	-5 / +15	L-Asn \cdot H ₂ O, 90-125
L3	30	94	2500	-5 / +10	L-Asn \cdot H ₂ O, 90-125
Val-DL1	35	241	2400	-8/0/-10 /+24/-12	L-Asn \cdot H ₂ O, 90-125
Val-DL2	35	241	2340	-4	D-Asn \cdot H ₂ O, 90-125
Val-L1	35	118	2500	-8/0/-10/ +17/-	L-Asn \cdot H ₂ O, 90-125
14/+27					

Complete dissolution of the solid feed material ($m_{\text{sat,Asn}\cdot\text{H}_2\text{O}}$, Table 2) was ensured by keeping the initial solutions 10K above saturation temperature for at least 1h. Afterwards, linear cooling was initiated at different rates ($\Delta T/\Delta t$, Table 2) and seed material was added after the prepared solutions were slightly subcooled ($\Delta T \approx 1\text{K}$). The utilized cooling rates were adjusted to yield moderate supersaturations causing significant growth and nucleation but no massive burst of nuclei, which would complicate subsequent analysis.

Seeds were prepared directly from the L-Asn·H₂O feed stock by careful sieving (fraction 90-125 μm) and the initial crystal mass was fixed at 2.6g (around 1% of the expected product mass of an Asn-crystallization with $T_{\text{sat}} = 45^\circ\text{C}$ and $T_{\text{cryst}} = 20^\circ\text{C}$). D-Asn·H₂O seeds were prepared by a recrystallization of the mother liquors from Preferential Crystallizations of DL-Asn. The seed size, i.e. the sieve fraction (90-125 μm), and mass (2.6g) was the same as for the L-Asn·H₂O seed material.

Online recording of the density was initiated after solid feed material was added to follow the overall concentration evolution. Offline samples for liquid composition analysis by HPLC were withdrawn every 6-7min shortly before seed addition and greyscale videos (30s at 20fps) were collected by online microscopy every 2-3 min following seeding.

All experiments were interrupted after a certain size of the grown seeds was achieved to prevent blockage or sedimentation inside the online microscope. Products of the Preferential Crystallizations (Exp. DL1-DL4 and Val-DL1, Table 2) were subsequently withdrawn, filtered and washed with an ethanol/ water-mixture (40/60 wt-%) to prevent nucleation in the adherent mother liquor or dissolution of the crystals. The crystallized material was finally sieved and each fraction analyzed with respect to purity and structural identity.

Product suspensions of the pure L-asparagine experiments (L1-L3, Table 2) remained in the crystallizer and were heated again to study the dissolution kinetics. The linear heating rates were chosen to yield significant undersaturation but even with 20 K/h, which was close to the technical limit of the setup, only small driving forces for dissolution were achieved, complicating the final estimation of the kinetic parameters. The online sampling procedure (online density, online microscopy) was the same as for the crystallization part of the experiments.

Three different validation experiments were carried out after estimation of the crystallization kinetics (Val-DL1, Val-DL2 and Val-L1, Table 2). Several linear cooling and heating ramps, different from the previous experiments, were combined to evaluate the estimates at varying conditions. Only the second validation was carried out with one constant cooling rate to compare growth of D-Asn·H₂O seeds to the one of the L-enantiomer.

3. Estimation and validation procedure

3.1. Driving force calculation in a ternary system

Preferential Crystallization is essentially an instable process carried out in the supersaturated, metastable region of the ternary phase diagram (blue region in Fig. 4). Addition of enantiopure crystals to a racemic liquid phase (50/ 50 D- and L-enantiomer, thin dashed line in Fig. 4) yields a selective removal of this specific enantiomer from the motherliquor until the antipode nucleates. Afterwards, both species grow simultaneously until equilibrium conditions are reached, i.e. until both, the solid and liquid are of racemic composition. A change in the liquid phase composition will alter the driving force of both stereoisomers, which needs to be considered in the calculation of the supersaturation to describe a Preferential Crystallization

appropriately. Additionally, a supersaturation calculation dependent on the liquid phase composition is essential to compare and evaluate kinetic experiments from racemic and enantiopure solutions. The theory will be explained in the following on the example of a chiral hydrate forming system shown in figure 4.

The driving force is formed by the chemical potential of one particular enantiomer in the current state of the system and the respective equilibrium or saturated state (e.g. the solubility isotherms $x_{\text{sat,D-H}_2\text{O}}$, $x_{\text{sat,L-H}_2\text{O}}$ in Fig. 4). However, equilibrium conditions must be avoided during a Preferential Crystallization, since the liquid phase state is then at racemic composition at the intersection of both isotherms and the separation was not successful. The state of the liquid phase needs to be kept in the metastable three-phase region (e.g. $x_{i,0}(t)$ in Fig. 4). A saturation or equilibrium state does not exist for the supersaturation calculation in this area and, hence, the extensions of the solubility isotherms are utilized as the reference state [25]. They are termed metastable solubility isotherms (bold dashed lines in the blue area, Fig. 4) and are calculated by extrapolating the solubility isotherms into the three-phase area. The corresponding reference state for the current state of the system ($x_{i,0}$) is, thus, given by the extension of the lines connecting the pure phase corners with the actual state ($\overline{\text{L} \cdot \text{H}_2\text{O} x_{i,0}}$, $\overline{\text{D} \cdot \text{H}_2\text{O} x_{i,0}}$, red and blue dotted lines in Fig. 4) to the metastable saturation isotherms (red and blue dots in Fig. 4). The ratio between the chemical potentials of the current (green dot, Fig. 4) and the individual reference state (red or blue dot, Fig. 4) is a measure for the driving force of crystallization of each enantiomer. Nevertheless, for the calculation of the supersaturation (eq. 1), only mass fractions of the states are used instead of the chemical potential, which is sufficiently accurate for most engineering purposes.

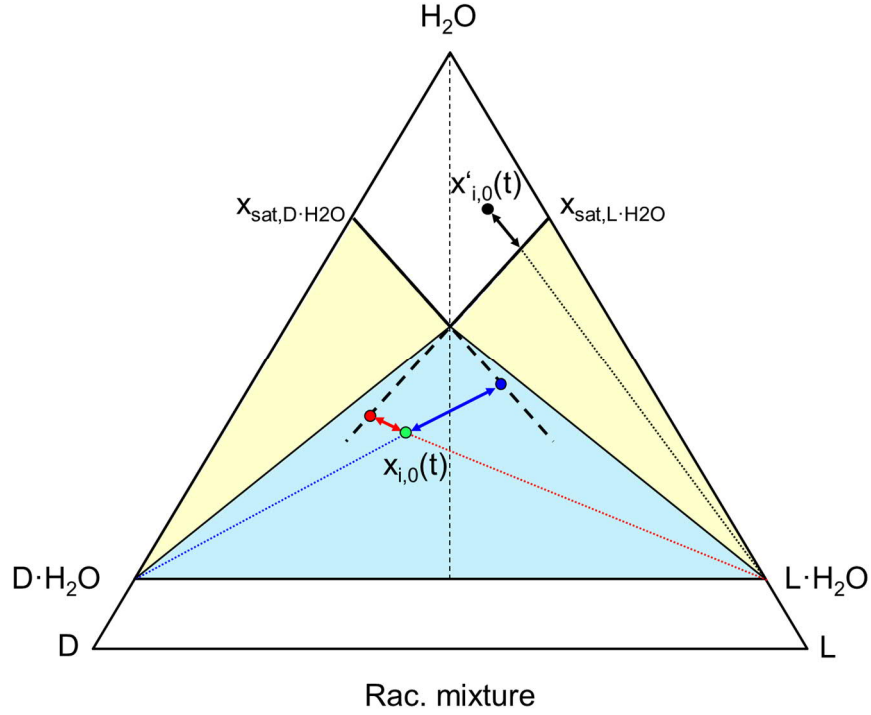


Fig. 4: Ternary phase diagram of two hydrate forming enantiomers ($L \cdot H_2O$ and $D \cdot H_2O$) and water at a certain temperature. A supersaturated, slightly D-enriched liquid state (green dot, $x_{i,0}$) and an undersaturated, slightly L-enriched liquid state (black dot, $x'_{i,0}(t)$) is indicated. The supersaturation for each enantiomer for the state $x_{i,0}(t)$ is depicted as the distance (blue and red double-arrows) between the actual state (green dot) and the corresponding extension of the solubility isotherm (black dashed lines). For the sake of clarity, only the L-undersaturation is depicted as the distance between ($x'_{i,0}$) and the solubility isotherm (black solid lines $x_{sat,D \cdot H_2O}$, $x_{sat,L \cdot H_2O}$). White, yellow and blue areas mark the one-, two- and three-phase domains of the monohydrate, respectively.

It should be noted, that the ratio between the mass fractions of the opposite enantiomer and the solvent are constant along lines $\overline{L \cdot H_2O x_{i,0}}$ and $\overline{D \cdot H_2O x_{i,0}}$ (isopleths), which needs to be

considered in the determination of the corresponding reference states ($x_{\text{sat},i}$) located on the metastable solubility isotherms (blue and red dots on the bold dashed lines in Fig. 4). The supersaturation of the monohydrate of an enantiomer i ($i = \text{D}\cdot\text{H}_2\text{O}, \text{L}\cdot\text{H}_2\text{O}$) is therefore expressed by eq. 1 where the denominator describes the calculation of the saturated state based on the actual temperature (T).

$$S_i(T) = \frac{x_{i,0}}{x_{\text{sat},i}(T)} \quad \text{for } i = \text{D}\cdot\text{H}_2\text{O}, \text{L}\cdot\text{H}_2\text{O} \quad (\text{eq. 1})$$

In this study, the investigation of kinetics is based on polythermal seeded batch-crystallizations, where the driving force is dynamically changing due to changes of temperature, T , and composition, x_i . Hence, a transient supersaturation calculation is utilized given by eq. 2.

$$S_i(t, T, x_i) = \frac{x_{i,0}(t)}{x_{\text{sat},i}(T(t), \frac{x_{j,0}(t)}{x_{\text{Solvent},0}(t)})} \quad \text{for } i = \text{D}\cdot\text{H}_2\text{O}, \text{L}\cdot\text{H}_2\text{O} \text{ and } j = \text{D}\cdot\text{H}_2\text{O}, \text{L}\cdot\text{H}_2\text{O} \neq i \quad (\text{eq. 2})$$

where the denominator describes additionally the ratio between the mass fraction of the counter-enantiomer and the mass fraction of the solvent. In case of dissolution, eq. 2 can be utilized to calculate the undersaturation as well (depicted as black double arrow for the undersaturated state $x'_{i,0}$ (black dot) in Fig. 4).

Polynomial functions (eq. 3) were fitted to solubility data from [21] using precomputed simplex algorithms from MatLab. The resulting solubility surface parameters are summarized in table 3. They are identical for D- and L-asparagine monohydrate because of the mirror-symmetry of enantiomers and were utilized subsequently to calculate the driving force for all experiments from the recorded temperature (T) and the transient liquid composition.

$$x_{\text{sat},i}(t, T, x_i) = K_1 + K_2 \cdot T(t) + K_3 \cdot T(t)^2 + K_4 \cdot \frac{x_j(t)}{x_{\text{Solvent}}(t)} \quad (\text{eq. 3})$$

for $i = \text{D} \cdot \text{H}_2\text{O}, \text{L} \cdot \text{H}_2\text{O}$ and $j = \text{D} \cdot \text{H}_2\text{O}, \text{L} \cdot \text{H}_2\text{O} \neq i$

Table 3: Solubility parameters for description of the ternary solubility surfaces (Fig. 2) of L- and D-asparagine monohydrate using equation 3 based on data of [21].

Parameter	L-/ D-Asn·H ₂ O	Unit
K ₁	0.0104	-
K ₂	1.0584x10 ⁻⁴	1/°C
K ₃	2.4432x10 ⁻⁵	1/°C ²
K ₄	0.0312	-

3.2. Data evaluation and parameter estimation

Figure 5 shows an example of the recorded liquid phase data from experiment DL2 (Table 2). L-Asn·H₂O seeds were introduced to the slightly supersaturated solution at $t = 0\text{h}$ subsequent to the start of the linear cooling (brown line in Fig. 5). A reduction of the L-Asn mass fraction starts first after $\approx 0.7\text{h}$ while D-Asn remains constant in the liquid phase (red dots and line in Fig.6).

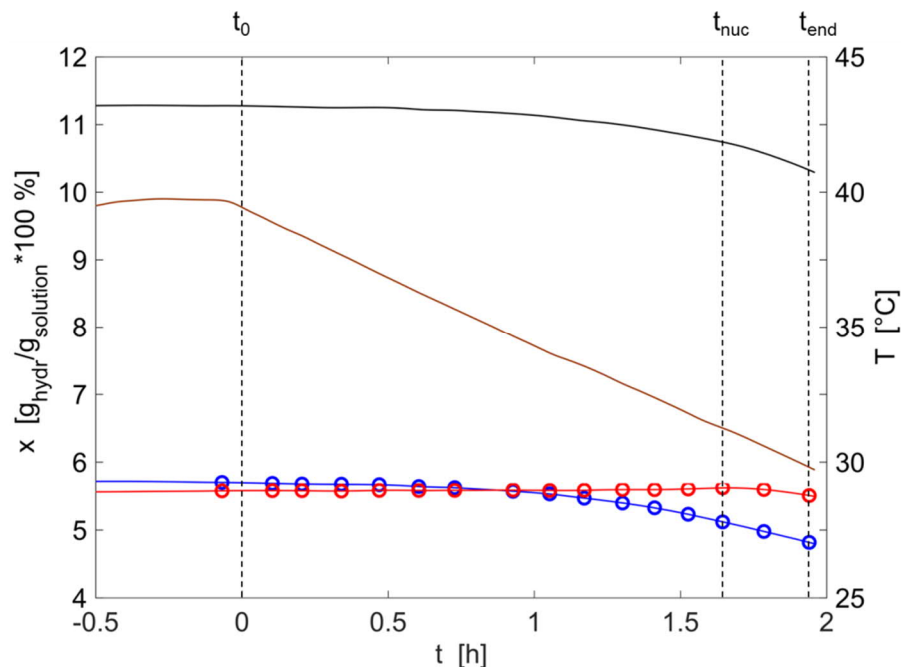


Fig. 5: Trajectories of the liquid state of experiment DL2. Black line - total concentration of asparagine calculated from the calibrated density signal; Brown line - temperature; Blue and red dots - measured concentration of dissolved L- and D-Asn·H₂O by HPLC; Blue and red line - interpolation of HPLC results for L- and D-Asn·H₂O.

The liquid phase composition of the same experiment is shown in figure 6 by means of the ternary phase diagram of asparagine monohydrate. It is clearly visible, that the initial solution (purple dot at t_0) is slightly L-Asn enriched caused by a non-racemic feed material. However, the asymmetry, which is below 0.15 wt-%, is irrelevant for the kinetic investigations since it is considered in the supersaturation calculation. After seeding at $t = t_0$, the solution enriches with respect to D-Asn along the connection line to the pure L-Asn·H₂O triangle corner (blue dotted line in Fig. 6) showing selective crystallization of the seeded enantiomer. The antipode starts to nucleate at $t = t_{\text{nuc}}$, which changes the trend of the liquid phase evolution towards racemic

conditions. Hence, the measured quantities are in perfect agreement with the expected behavior of Preferential Crystallization indicating the quality of the setup. Further processing of the suspension would lead to a 50/50 composition in the liquid phase at the final temperature, T_{cryst} (purple dotted line, Fig. 6). The experiment was interrupted at t_{end} to prevent sedimentation of larger crystals inside the online microscope, followed by solid-liquid separation of the suspension and washing of the product crystals (section 2.6).

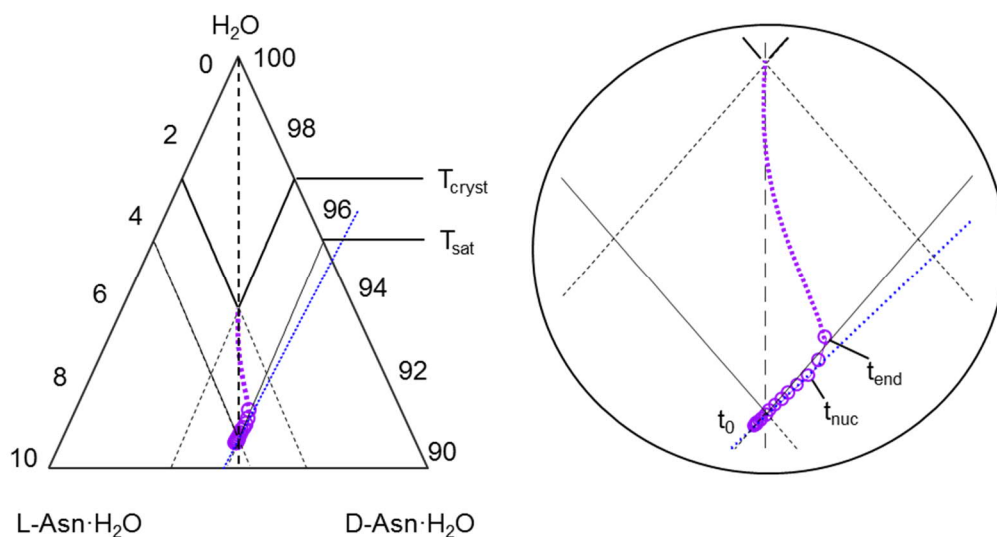


Fig. 6: Transient mass composition of experiment DL2 shown by means of the ternary phase diagram of asparagine monohydrate (only a part of the ternary phase diagram shown). Purple dots and solid line - measured composition and interpolated trajectory of the liquid phase; Black solid lines - solubility isotherms at T_{sat} and T_{cryst} ; Blue dotted line - connection to pure L-Asn·H₂O corner; Purple dotted line - calculated trend of the experiment after t_{end} .

The crystal size evolution is extracted from the grey-scale images recorded by the online microscopy complementary to liquid phase analysis. An image processing routine [23] is utilized for this purpose, which mainly consists of an automatic background subtraction, region filling and binarization by a global grey-scale threshold. Afterwards, it is straightforward to extract the dimensions and characteristic shape factors, like sphericity and convexity, of the observed objects from the generated black and white pictures. The shape factors are exploited subsequently to distinguish single-particles from agglomerates and air bubbles. Figure 7 a) depicts an online-microscopic picture of the observed objects and the selection of the relevant crystals.

From the identified single crystals, the minimal Feret diameter (exemplary shown in Fig. 7 b) is used as characteristic length, L , to describe the CSD evolution in the following since it is well comparable to results of a sieve analysis. Together with the maximal Feret diameter a volume shape factor, k_v , necessary for the PBE model can be derived, which relates the volume of a cube to the volume of the prismatic asparagine crystals.

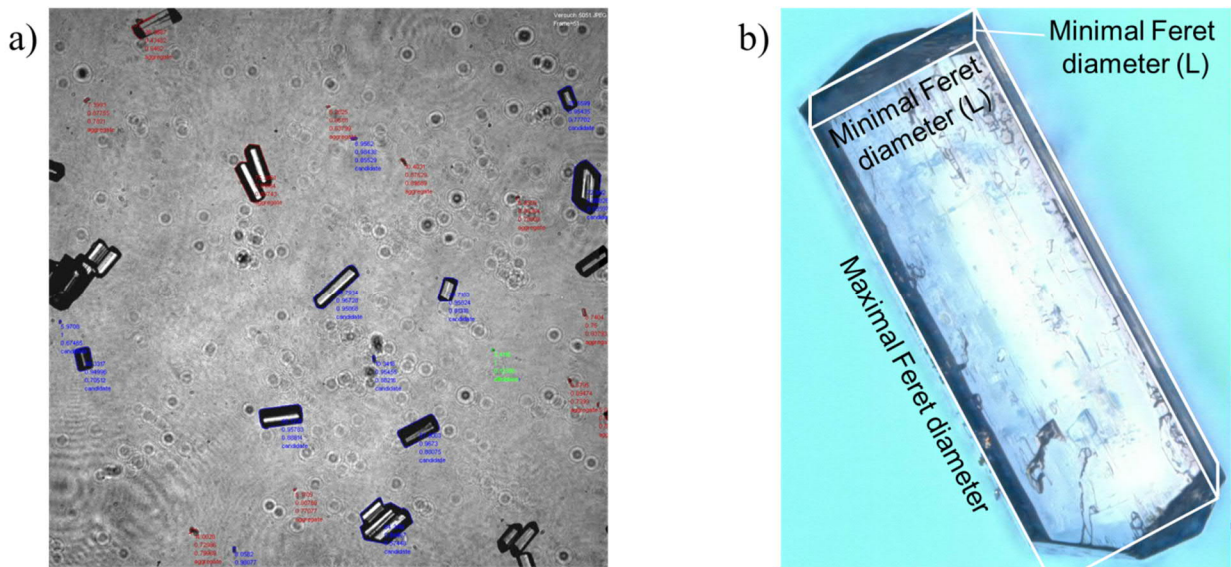


Fig. 7: a) Online-microscopy image of experiment DL2 (Table 2). b) Image of an asparagine monohydrate crystal in comparison with the assumed square based prismatic shape. The dimensions measured by the online microscope are indicated.

Figure 8 shows an example of a typical trend of the size distribution for a crystallization-dissolution experiment from pure L-asparagine solution. The initially present seed crystals start to grow while temperature is lowered and hence, supersaturation is generated (Fig. 8 a) for $t = 0 \dots 1.7\text{h}$). Additionally, it can be seen, that the amount of fines increases due to nucleation during this period as well (population in the size range of $0\text{-}50\mu\text{m}$, Fig. 8 a). At a mean seed crystal size of $250\mu\text{m}$ at $t = 1.7\text{h}$ (Fig. 8 a), heating of the suspension is initiated causing a fast dissolution of the present solid phase until at the end of the experiment ($t = 2.4\text{h}$) only a clear solution remains.

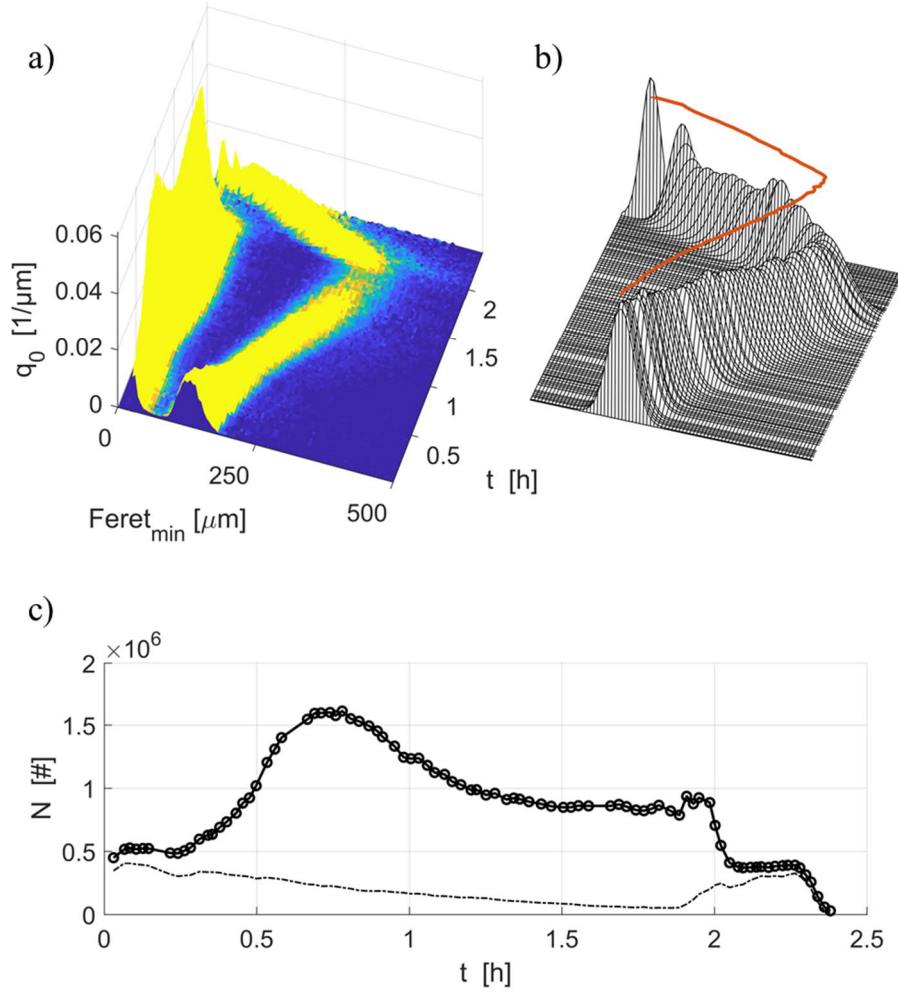


Fig. 8: a) Crystal size evolution during experiment L1 measured by the online microscope. b) Extracted seed crystal distributions and mean seed size evolution. c) Volume related total single-crystal number (solid line and circles) and number of seed crystals (dashed-dotted line) observed by the online microscope.

The movement of the seed peak over time is a consequence of the driving force and kinetics of growth and dissolution. Hence, the mean size evolution of this seed population can be utilized together with the liquid phase state to estimate parameters of suitable kinetic approaches. However, a direct calculation of the mean seed crystal size from all measured distributions is

challenging due to the upcoming nuclei or, if present, agglomerates and broken particles. Hence, a Gaussian distribution, which reflects the initial seed distribution, is fitted to the seed peak of all measurements (compare Fig. 1 and black lines in Fig. 8 b). The mean values of these distributions (red line in Fig. 8 b) correspond hence only to the mean size of the seed population. A detailed description of this procedure can be found in [14].

Simultaneously, all single crystals are counted, which are observed by the online microscope. It can be seen from figure 8 c) (solid line and circles), that after the seed addition ($t = 0\text{h}$) the total number of crystals increases steadily due to secondary nucleation until a certain plateau is reached ($t \approx 0.7\text{h}$). At this point, the suspension density increased to a level, which causes particle overlapping on the acquired image data. These particles are then labeled as agglomerates and are not processed further, which reduces in sum the total amount of measured crystals. Hence, only the first increase of the crystal number (until $t = 0.7\text{h}$) can be exploited for estimation of the secondary nucleation kinetics. Nevertheless, seed crystals are still identified in a sufficiently large number (dashed-dotted line in Fig. 8c), which allows for good identification of the seed-peak.

From these explanations it becomes clear, that only characteristic parts of the data of all experiments can be utilized for estimation of the crystallization kinetics as depicted in Fig. 9 for experiment L1 (Table 2). For growth, only data is taken where supersaturation is present and a positive change of the mean size is visible (blue boxes in Fig. 9). Similarly, undersaturation and a decrease of the crystal size are necessary to estimate parameters for a dissolution kinetics (orange boxes in Fig. 9). Secondary nucleation kinetics are estimated from, again, supersaturated conditions and an increase of the single-crystal number where particle overlapping is not detected (green boxes in Fig. 9).

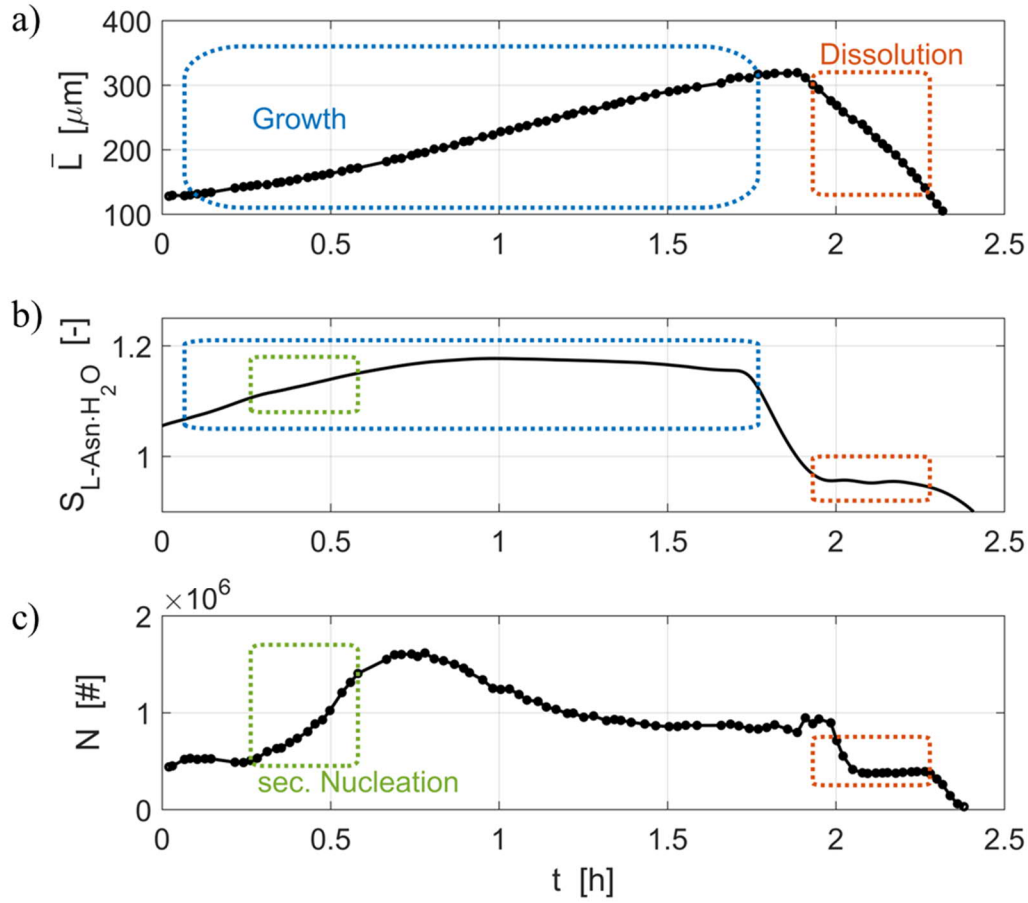


Fig. 9: Data of experiment L1 with indication of areas, which were taken for the subsequent parameter estimation. a) Mean seed crystal size. b) Driving force with respect to L-Asn. c) Volume-related crystal number evolution.

The chosen datasets of all experiments that starting from racemic liquid phase composition (DL1-DL4, Table 2) are subsequently utilized to estimate growth kinetics. Datasets of all experiments with pure L-Asn solutions (L1-L4, Table 2) served to estimate growth, nucleation and dissolution kinetics. The respective parameters were fitted via a least-square method satisfying the objective functions eq. 4-9 [14].

$$OF_G = \sum_{j=1}^{n_{Exp}} \sum_{i=1}^{n_{datapoints}} \left(\bar{L}_{sim,i,j} - \bar{L}_{meas,i,j} \right)^2 \quad \text{for } S \geq 1 \quad (\text{growth}) \quad (\text{eq. 4})$$

$$OF_B = \sum_{j=1}^{n_{Exp}} \sum_{i=1}^{n_{datapoints}} \left(N_{sim,i,j} - N_{meas,i,j} \right)^2 \quad \text{for } S \geq 1 \quad (\text{nucleation}) \quad (\text{eq. 5})$$

$$OF_D = \sum_{j=1}^{n_{Exp}} \sum_{i=1}^{n_{datapoints}} \left(\bar{L}_{sim,i,j} - \bar{L}_{meas,i,j} \right)^2 \quad \text{for } S < 1 \quad (\text{dissolution}) \quad (\text{eq. 6})$$

$$\bar{L}_{sim} = \bar{L}_{seed} + \int_0^t G \, dt \quad \text{for } S \geq 1 \quad (\text{eq. 7})$$

$$N_{sim} = N_{seed} + \int_0^t B_0 \, dt \quad \text{for } S \geq 1 \quad (\text{eq. 8})$$

$$\bar{L}_{sim} = \bar{L}_{S<1} - \int_0^t D \, dt \quad \text{for } S < 1 \quad (\text{eq. 9})$$

Different kinetic approaches are fitted to the datasets to identify the most suitable one with the least amount of parameters. The general structure of the mathematical approaches is represented by equation 10, which is used with one ($p_2 = \text{const.} = 1$, $p_3 = \text{const.} = 0$), two ($p_3 = \text{const.} = 0$) or three adjustable parameters. Additionally, a secondary nucleation kinetics ($B_{0,sec,i}$) is tested (eq. 11), which should describe the nucleation mechanism better due to the suspension density dependency. At least 1×10^5 parameter estimations were carried out for each approach with randomly generated initial values due to the known correlation of parameters in power-law equations.

$$K_i = p_i \exp\left(\frac{-p_3}{RT}\right) (S_i - 1)^{p_2} \quad \text{for } K = G, D, B_0 \text{ and } i = D-, L\text{-Asn} \cdot H_2O \quad (\text{eq. 10})$$

$$B_{0,sec,i} = p_i \left(S_i(T) - 1 \right)^{p_2} \rho_{susp}^{p_3} \quad \text{for } i = D-, L\text{-Asn} \cdot H_2O \quad (\text{eq. 11})$$

3.3. Validation procedure

After parameter estimation, different validation experiments (Val-DL1,2 & Val-L1, Table 2) are carried out to evaluate the identified kinetics. A full population balance model is utilized for this purpose equipped with the kinetic approaches to compare experimental observations with simulation results.

$$\frac{\partial f_i(t, L)}{\partial t} = - G_i(S_i(t), T(t)) \frac{\partial f_i(t, L)}{\partial L} \quad \text{for } S_i \geq 1 \text{ and } i = D, L \quad (\text{eq. 12})$$

The simple model for crystallization ($S_i \geq 1$) of the two enantiomers, i , ($i = D, L$) assumes that breakage and agglomeration are negligible, the growth rate is size independent and ideal mixing without volume contraction due to an evolving solid phase [1] holds. Supersaturation, S_i , is calculated for both species by eq. 2 according to the liquid phase composition that is described by three mass balances (eqs. 13 & 14) for the components of the system (L-Asn·H₂O, D-Asn·H₂O, H₂O). It should be noted, that the solvent mass balance considers only the loss of water due to the formation of asparagine monohydrate, which is the stable solvate under the given experimental conditions.

$$\frac{dm_i(t)}{dt} = - 3k_v \rho_{solid} G_i(S_i(t), T(t)) \int_{L_{min}}^{L_{max}} L^2 f_i(t, L) dL \quad \text{for } i = D-, L\text{-Asn} \cdot H_2O \quad (\text{eq. 13})$$

$$\frac{dm_{H_2O}(t)}{dt} = \left(\sum_i - 3k_v \rho_{solid} G_i(S_i(t), T(t)) \int_{L_{min}}^{L_{max}} L^2 f_i(t, L) dL \right) \frac{M_{H_2O}}{M_{Asn \cdot H_2O}} \quad \text{for } i = D-, L\text{-Asn} \cdot H_2O$$

(eq. 14)

Simulations are carried out with initial conditions equal to the starting process values (Table 2) of the validation experiments. The seed distribution (eq. 15) is taken from the first evaluated online microscope images and the liquid phase compositions (eq. 16) are based on the weighed-in feed masses of the components.

IC for $S_i > 1$:

$$f_i(t=0, L) = f_{\text{seed, meas}}(L) \quad \text{for } i = \text{D-}, \text{L-Asn} \cdot \text{H}_2\text{O} \quad (\text{eq. 15})$$

$$m_i(t=0) = m_{i, \text{meas}}^0 \quad \text{for } i = \text{D-}, \text{L-Asn} \cdot \text{H}_2\text{O}, \text{H}_2\text{O} \quad (\text{eq. 16})$$

$$f_i(t, L=0) = \frac{B_{0,i}}{G_i} \quad \text{for } i = \text{D-}, \text{L-Asn} \cdot \text{H}_2\text{O} \quad (\text{eq. 17})$$

In case of dissolution ($S_i < 1$), G_i is exchanged by D_i in eqs. 12-14 with an adjusted boundary condition (eq. 17) to describe the loss of particles [14]. The model (eqs. 10-17) was implemented in MatLab and numerically solved using a pre-programmed Runge-Kutta method of 4th order. All experiments were simulated for 10s time steps and 2000 elements of the length coordinate, which was discretized equidistantly between 1 μm and 2 mm.

4. Results

4.1. Parameter estimation

Figure 10 depicts the data utilized for estimation of the growth kinetics of L-Asn·H₂O crystals in racemic solutions (G_{DL}). All experiments were interrupted at similar mean widths of the seed fraction of around 260μm to prevent sedimentation or blockage of the online microscope bypass (Fig. 10 c) causing different experimental times. The seed crystals in DL1 were grown for nearly 3h before the target size was reached where in DL2 only 2h were necessary. The measured transient L-Asn·H₂O supersaturations of each experiment are depicted with time in Fig. 10 a) and with temperature in Fig. 10 b). The observed maximal L-Asn·H₂O supersaturations differ significantly from $S_{L-Asn \cdot H_2O} = 1.3$ (Fig. 10 a), DL2, $T_{sat} = 40^{\circ}C$) to $S_{L-Asn \cdot H_2O} = 1.45$ (Fig. 10 a), DL4, $T_{sat} = 30^{\circ}C$) even though the same cooling rates were used for DL2, DL3 and DL4 (- 5 K/h, Table 2).

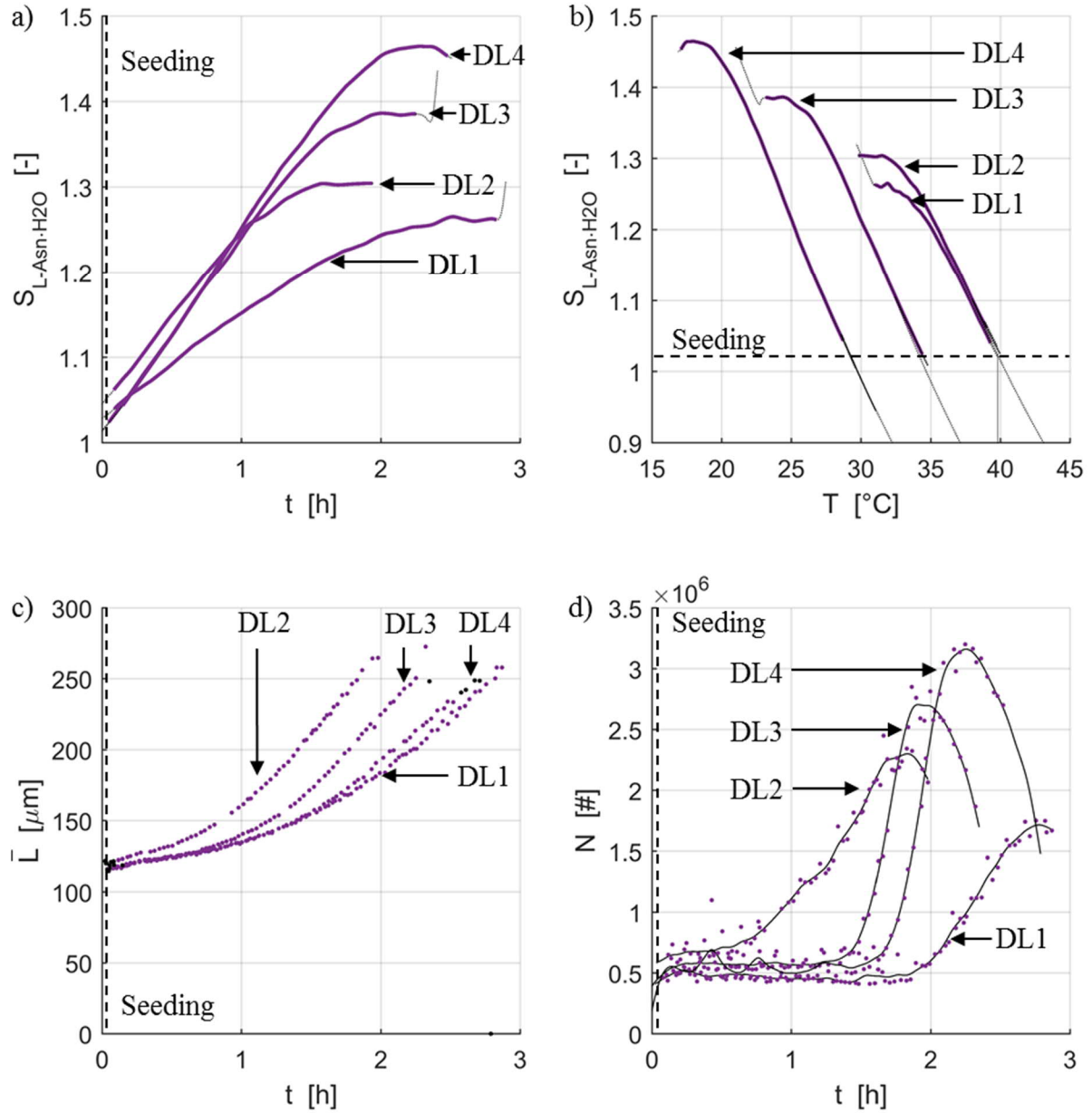


Fig. 10: Dataset of all Preferential Crystallizations of L-Asn-H₂O from racemic liquid phases (DL1-DL4, compare Table 2) utilized for the estimation of the growth kinetics. a) Transient supersaturation. b) Transient supersaturation as a function of temperature indicating the range of validity for the parameter estimates. b) Mean size evolution of the seed fraction evaluated as described in section 3.2. d) Crystal number evolution with time.

Similar trends can be seen with respect to nucleation (Fig. 10 d). The single particle number increases earlier during DL2 (at 0.7h) compared to DL4 (at 1.4h) indicating a nonlinear correlation between kinetics and the crystallization temperature and supersaturation. In general, however, both kinetics, nucleation and growth, are proportional to the respective process condition. For example, during experiment DL1 with a lower cooling rate (-3 K/h, compare Table 2) the lowest level of supersaturation (Fig. 10 b), DL1, $T_{\text{sat}} = 40^{\circ}\text{C}$, $S_{\text{L-Asn}\cdot\text{H}_2\text{O}, \text{max}} \approx 1.25$) and only moderate nucleation (Fig. 10 d), DL1) were measured but the longest experimental duration was necessary to grow the seed crystals to their final size.

It should be noted, that the increase of detected particles results from two mechanisms due to the different conditions for both species. Primary nucleation of the counter enantiomer (D-Asn) occurs due to the high supersaturation of the antipode and secondary nucleation of the preferred enantiomer, since already a crystalline phase of this component is present. In figure 11 the sieve analysis of the DL2 product is depicted together with the purity analyses of each sieve fraction. The grown nuclei (sieve fraction $< 200\mu\text{m}$) consist only of 20% of L-Asn·H₂O originating from secondary nucleation. Most of these fractions is D-Asn·H₂O indicating strong primary nucleation early in the experiment. Small impurities in the seed-fraction are only caused by agglomeration of these crystals with grown nuclei, formed during the washing procedure.

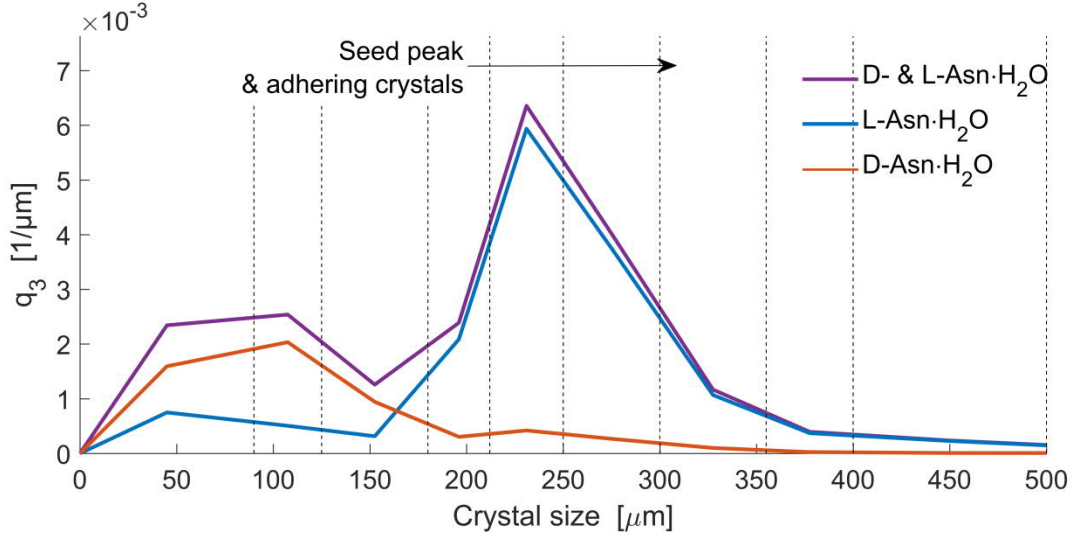


Fig. 11: Sieve analysis of experiment DL2 product combined with the results of the purity analyses of each sieve fraction to reconstruct the underlying L- and D-distributions. Dashed lines - sieve classes.

Experiments from pure L-Asn solutions (Fig. 12) were started under conditions similar to the Preferential Crystallizations from racemic liquid phases. Saturated solutions were prepared at the same temperatures and cooled at the same rates until a ΔT was reached, comparable to experiments DL2 - DL4 ($\Delta T \approx 10\text{K}$, Fig. 12 b) to allow for an objective evaluation of both datasets. Subsequently to crystallization, heating was initiated resulting in undersaturation (orange curves in Fig. 12 b) and dissolution of the grown seeds (orange curves in Fig. 12 c). Different colors in figure 12 a) - d) indicate the data that was utilized to estimate afterwards the different crystallization kinetics as explained in section 3.2.

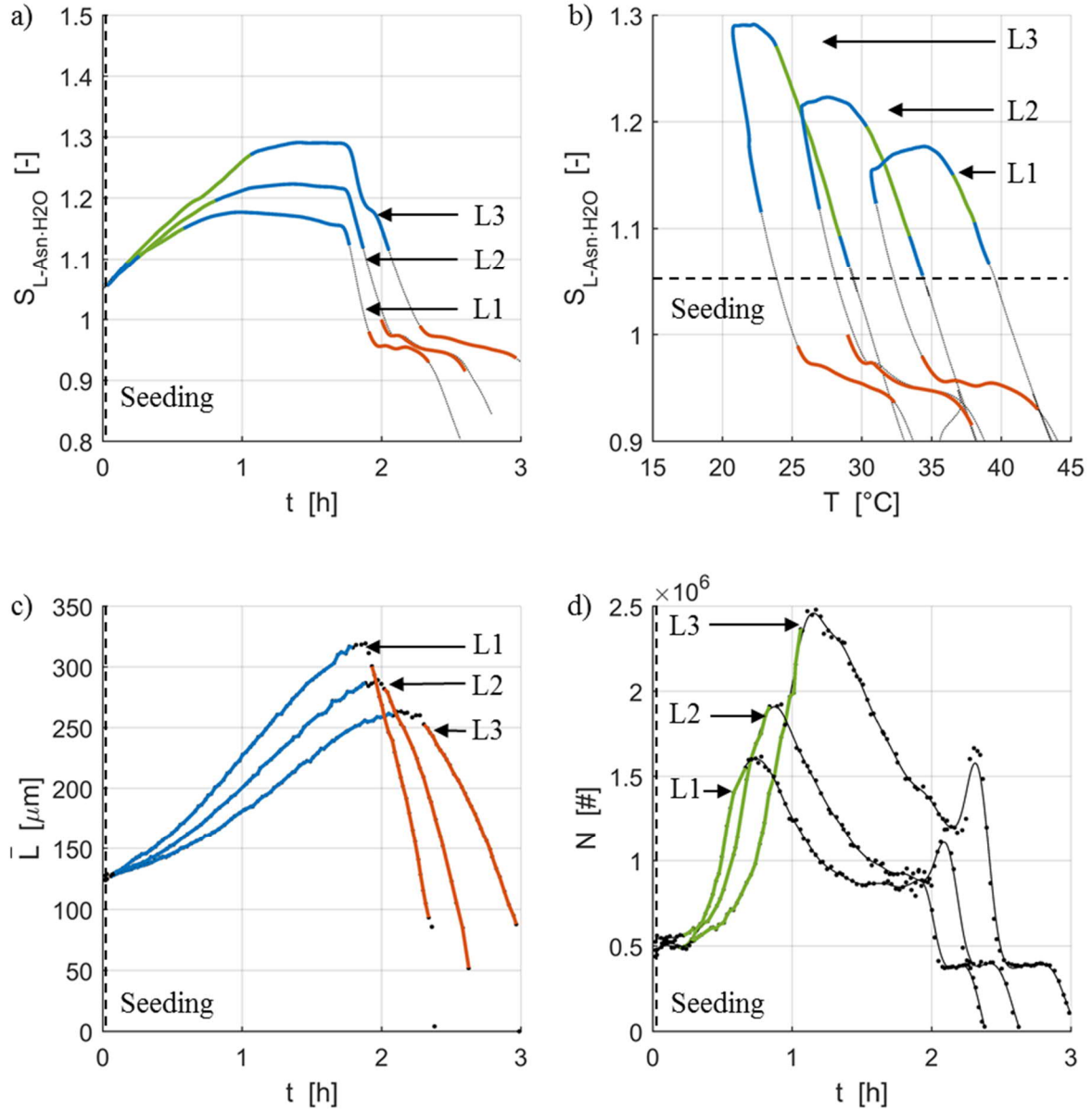


Fig. 12: Dataset of all experiments (L1-L3, compare Table 2) from pure L-Asn solutions utilized for estimation of growth, nucleation and dissolution kinetics. a) Transient super- and undersaturation. b) Measured temperatures and calculated supersaturation indicate the range of validity for the parameter estimates. c) Mean size evolution of the seed fraction evaluated as described in section 3.2. d) Crystal number evolution. Blue - data used for estimation of growth

kinetics; Green - data used for estimation of nucleation kinetics; Orange - data used for estimation of dissolution kinetics.

It becomes clear from figure 12 c), that the increase of the mean length is much higher without the counter enantiomer. The seed mean size increased after 1.5h to 225 μ m - 290 μ m in contrast to 155 μ m - 210 μ m in presence of D-Asn at the same time. Noteworthy is the change in slope of the mean length evolution of the DL-experiments before and after a size of 150 μ m (Fig. 10 c). A certain startup period can be recognized followed by a nearly linear increase in size, a behavior, which is far less pronounced during the pure L-experiments (Fig. 12 c). Since all conditions were similar between both sets of crystallization experiments, it can be concluded, that this is caused by the counter enantiomer acting similarly to an active additive, which hinders growth in the beginning of the process. However, a retardation of specific crystal faces cannot be detected since a significant morphological change was not visible (Fig. 13).

Due to the pronounced growth in pure L-Asn solutions, more dissolved mass is depleted with time resulting in lower supersaturations measured (Fig. 12 a) & b). Less nucleation is detected (green curves in Fig. 12 d) since no primary nucleation is present but the particle number increases for all L-Asn experiments earlier and in a narrower time span (0.25h - 0.5h for L1 - L3 and 0.7h - 1.8h for DL1 - DL4). There are two possible explanations for this observation. The crystal surface, the main source for secondary nucleation, increases significantly faster during the experiments from pure L-Asn solutions. Nuclei or attrition fragments, on the other hand, have to grow to a certain size to be detected as single particles ($\approx 20 \mu$ m) in order to contribute to the observed crystal number. Hence, seed crystals grown from enantiopure solutions yield a larger increase of secondary nucleation due to their fast increase in size and the corresponding nuclei

are detected earlier since the growth rate is also larger. An additional influence of the counter enantiomers presence to the secondary nucleation rate is probable but cannot be concluded based on the observed data.

Fast dissolution takes place almost instantaneously after the liquid phase becomes undersaturated (orange curves in Fig. 12 c). A correlation between heating rates and dissolution is barely visible. The maximal undersaturations reached, while still a solid phase was present, is for all experiments around 0.95 and the slopes of the decrease in size (orange curves in Fig. 12 c) are similar.

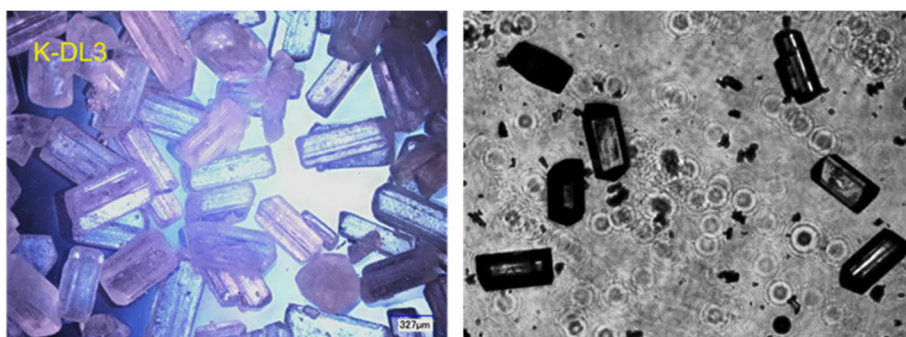


Fig. 13: Microscopic pictures of the products grown from racemic liquid phases (*left*) and online microscopic images of crystals grown from pure L-Asn solutions (*right*).

The parameters of the chosen kinetic expressions (eqs. 9 & 10) were estimated as explained in section 3.2 and are listed in table 4. It can be seen, that the approach with three adjustable parameters yields for all kinetics the lowest value of the objective function, as expected. Additionally, this approach reflects the previously discussed dependency of the kinetics to temperature and driving force. Only for the dissolution kinetics (D_L , Table 4), the correlation to the driving force is less pronounced ($p_3 = 0.51$), because of the small undersaturation range accessible for measurements. Surprisingly, the secondary nucleation approach (eq. 10,

$B_{0,sec,L-H_2O}$, Table 4) is outperformed by the power-law/ Arrhenius approach, which is maybe caused by the small range of data of suspension density and crystal number usable for the estimation.

Table 4: Parameter estimates of L-seed crystal growth kinetics grown from racemic solution and estimates for nucleation, growth and dissolution kinetics from pure L-Asn solution together with the corresponding minimal values of the objective functions (OF, eqs. 3-5). Marked kinetic parameters and approaches were utilized for simulations of the validation experiments. p_1 - kinetic pre-factor; p_2 - supersaturation exponent; p_3 - activation energy or suspension density exponent (eqs. 10 & 11).

Kinetics	OF minimum [m ² , -]	p₁ in [m/s, 1/s]	p₂ in [-]	p₃ in [kJ/mol, -]
Growth rate from DL-solutions, G_{DL} , (eq. 10)	1.1	5.92×10^{-8}	-	-
	9.2	3.33×10^{-8}	0.61	-
	0.5	8.43×10^6	2.47	76.74
Growth rate from L-solutions, G_L , (eq. 10)	4.0	1.27×10^{-7}	-	-
	12.0	2.34×10^{-8}	1.91×10^{-11}	-
	0.2	1.67×10^6	1.58	73.41
Dissolution rate from L-solutions, D_L , (eq. 10)	87.1	1.98×10^{-6}	-	-
	55.8	1.11×10^{-4}	2.24	-
	1.6	2.94×10^2	0.51	51.61
Nucleation rate from L-solutions, $B_{0,L}$, (eq. 10)	40×10^6	1.34×10^6	-	-
	35×10^6	2.59×10^5	0.09	-
	6×10^6	7.18×10^{25}	3.41	103.5
and $B_{0,sek,L}$, (eq. 11)	13×10^6	3.52×10^4	4.44×10^{-15}	2.305

The comparison of the growth rate from racemic (G_{DL} , Table 4) and pure L-Asn liquid phase (G_L , Table 4) illustrates the already discussed differences (Fig. 14). Growth rates from enantiopure solutions are 250% to 600% higher at supersaturations and temperatures between 1.1...1.3 and 25°C...40°C, respectively. Growth rates from DL-solutions are already close to zero at lower driving forces indicating the significant influence of the counter enantiomer in this range. In [19], the length evolution of L-Asn·H₂O from racemic and L-Asn solutions is measured with a single crystal growth cell. Additionally, the supersaturation calculation is different to the one introduced in section 3.1. Hence, a direct comparison of the growth rates estimated in this study to the results of [19] is not possible.

The estimated dissolution rates (D_L , Table 4, Fig. 15 a) are much faster than the growth rates given pure L-Asn solutions, as expected. Absolute values of both, the secondary nucleation ($B_{0,L}$, Table 4, Fig. 15 b) and dissolution rate, are in a range as detected for potassium dihydrogen phosphate, potassium alum or ortho aminobenzoic acid [15].

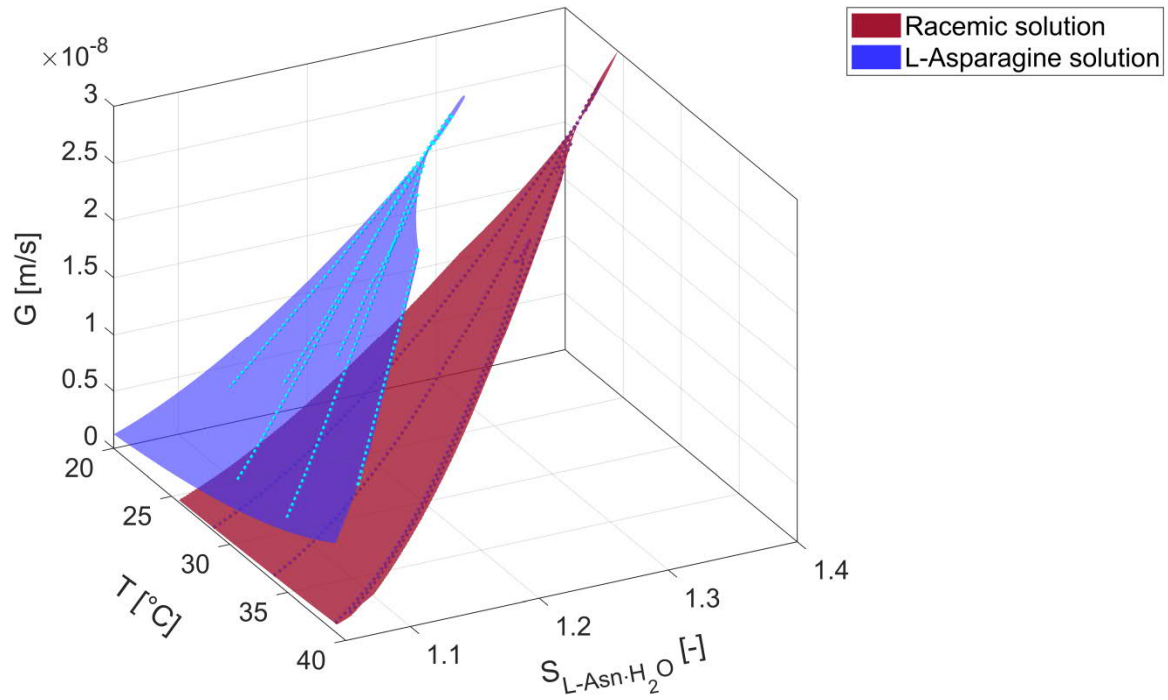


Fig. 14: Comparison of growth kinetics of L-Asn seed crystals from racemic and pure L-Asn solutions. Dotted lines - liquid state variables measured during the experiments DL1-DL4 and L1-L3 (compare Figure 10 & 12 and Table 2).

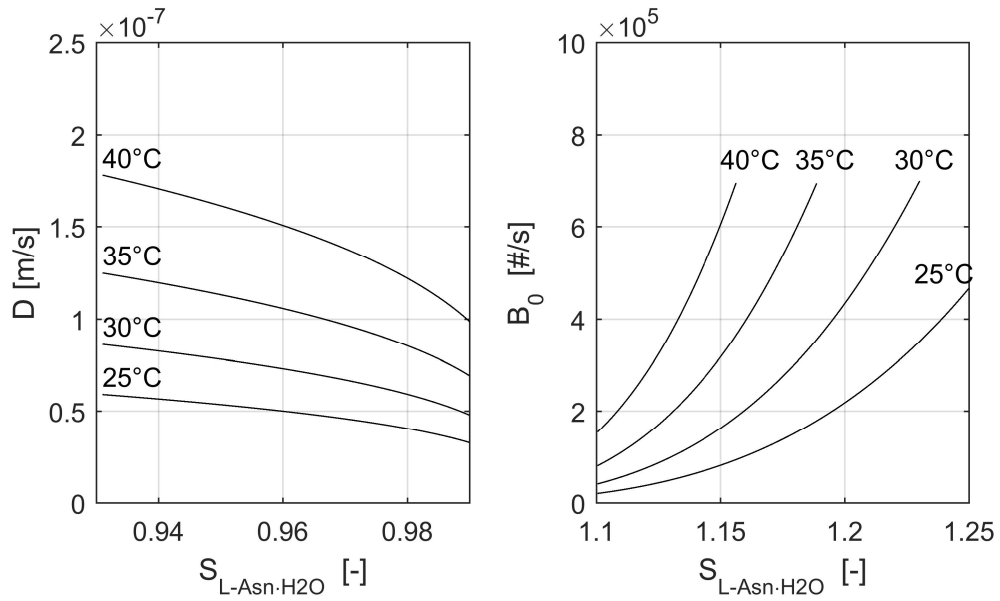


Fig. 15: Dissolution (D) and nucleation rate (B_0) of L-Asn from pure L-Asn solutions shown for different driving forces and temperatures.

4.2. Validation of the estimated kinetics

Validation experiments were carried out with different initial and process conditions for a comparison to simulations using the model described in section 3.3 in order to evaluate the quality of the kinetic parameter estimates. Figure 16 depicts the measured quantities of experiment VAL-DL1 (compare Table 2), which was started by seeding a slightly subcooled racemic solution saturated at 35°C with L-Asn crystals (sieve fraction 90 - 125µm).

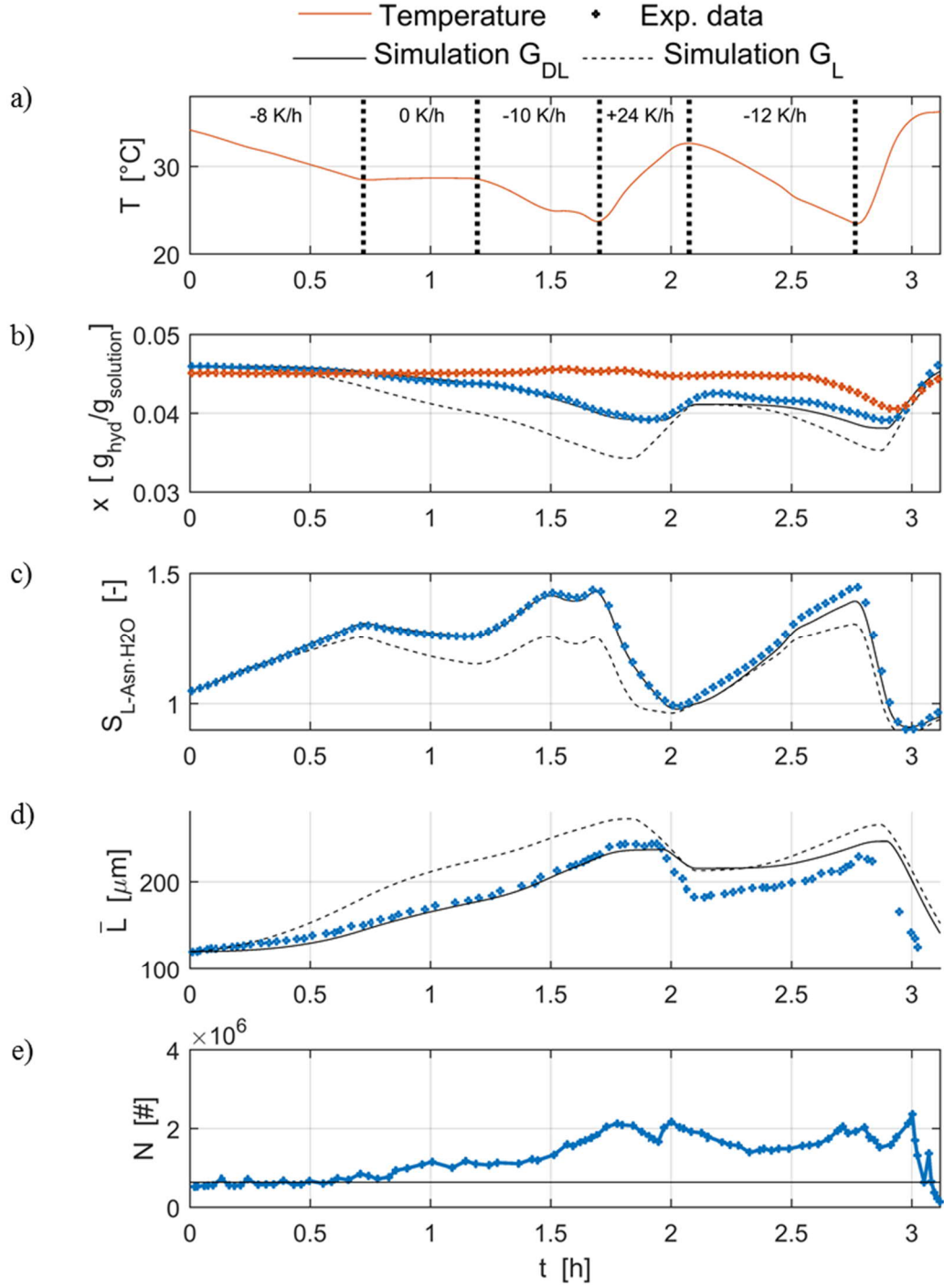


Fig. 16: Measured quantities of the validation experiment Val-DL1 in comparison with simulated values utilizing the previously estimated growth kinetics from racemic and pure L-Asn solutions. a) Temperature profile with indicated cooling and heating rates. b) Concentrations of

D- and L-Asn calculated from the overall Asn concentration and the HPLC analyses of the offline samples. c) Supersaturation profiles of both enantiomers. d) Mean seed crystal size evolution. e) Transient single particle number. Blue dots and curves - L-Asn; Red dots and curves - D-Asn; Black solid lines - simulation results applying the growth rate estimated from racemic solutions; Black dashed lines - simulation results applying the growth rate estimated from pure L-Asn solutions.

A more complex temperature profile (Fig. 16 a) was utilized subsequently to provoke different liquid states with respect to temperature-supersaturation combinations compared to the estimation experiments. The calculated transient concentration utilizing the growth rate estimated from DL-experiments (G_{DL} , Table 4, black solid line in Fig. 16 b) still agrees well with the measured profile. Only after the first heating cycle, small deviations occur.

To describe dissolution in this range, kinetics derived from the pure L-Asn experiments were applied. However, the mismatch (compare blue dots and black solid line at $t = 2\text{h}$ in Fig. 16 b) originates most certainly from erroneous solubility data. It becomes clear from the concentration profile and the mean crystal size evolution (black solid line in Fig. 16 d), that undersaturation is present at around $t = 2\text{h}$, which is not reflected by the driving force profile (black solid line in Fig. 16 c). Even a small relative error of 1% of the solubility surfaces (Fig. 2) yields 1-2% difference in driving force, which would explain the observations. Still, the trend following dissolution can be described with the PBE model quite well.

In contrary, significant deviations occur after a short time if the simulation is carried out with the growth rate estimated from pure L-Asn solutions (black dashed lines in Fig. 16) verifying again,

that kinetics are influenced by the presence of the counter enantiomer. It should be noted, that nucleation was not included in these simulation and will be discussed in the following.

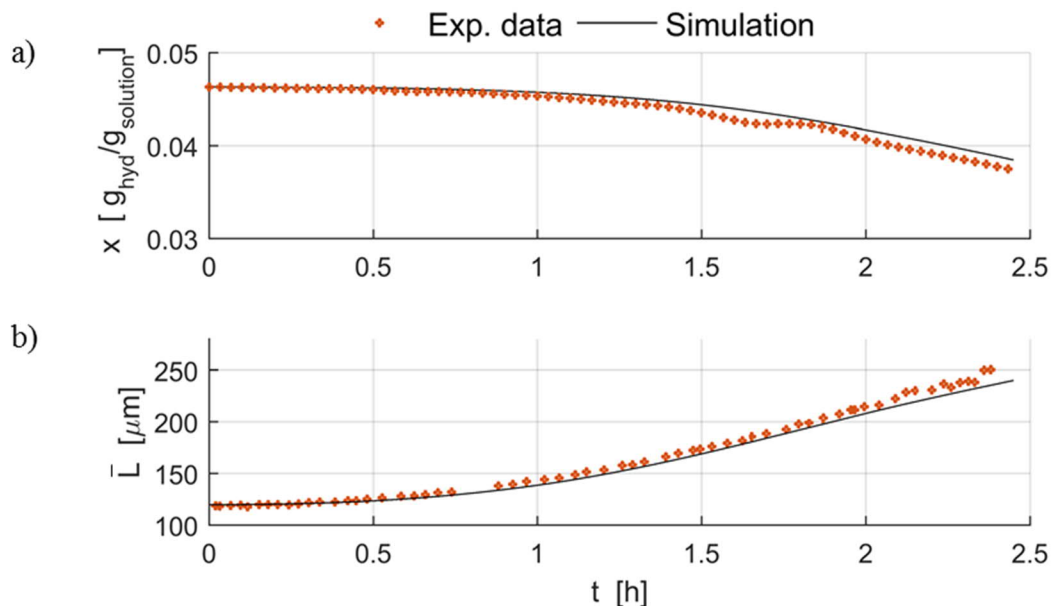


Fig. 17: Measured quantities of the validation experiment Val-DL2, started from racemic solution and seeded with D-Asn·H₂O, in comparison with simulated values utilizing the previously estimated growth kinetics from pure L-Asn solutions. a) Concentrations of D-Asn. b) Seed crystal mean size evolution.

Growth kinetics from experiments with racemic initial solutions, were utilized afterwards to also described crystallization of the counter enantiomer. A racemic solution saturated at 35°C was subjected to a simple linear cooling profile (compare Table 2) and subsequently seeded with D-Asn·H₂O. As seen from figure 17, both, concentration and length evolution can be described with great accuracy utilizing kinetics of L-Asn·H₂O (G_L & $B_{0,L}$, Table 4). Hence, it can be

concluded, that growth rates of both enantiomers in racemic solutions are the same in the considered range of supersaturation and temperature, as expected.

A third validation experiment serves to evaluate nucleation, growth and dissolution kinetics estimated from pure L-Asn solutions. Again, several cooling and heating cycles are used as for Val-DL1 (Fig. 18 a), Table 2). Comparison of the measured concentration and supersaturation with the simulated profile (black solid lines in Fig. 18 b) & c) shows a good agreement. Also the mean size of the seed crystals can be described well, even though, some small deviations occur after 1.5h in the range of the largest sizes reached (black solid line in Fig. 18 d). The nucleation kinetics in contrary cannot reflect the dynamics of the particle number precisely (black solid line in Fig. 18 e). Even though, the time point of the particle number increase agrees between the simulated and measured quantities, the slopes of both curves (compare blue and black solid lines in Fig. 18 e) differ significantly. To evaluate the impact of this deviation, a simulation is carried out neglecting secondary nucleation (black dashed lines in Fig. 18). It can be seen, that the influence of nucleation to the transient supersaturation and concentration is surprisingly small. Only the simulated seed crystal mean size increases above the measured values after 1.5h.

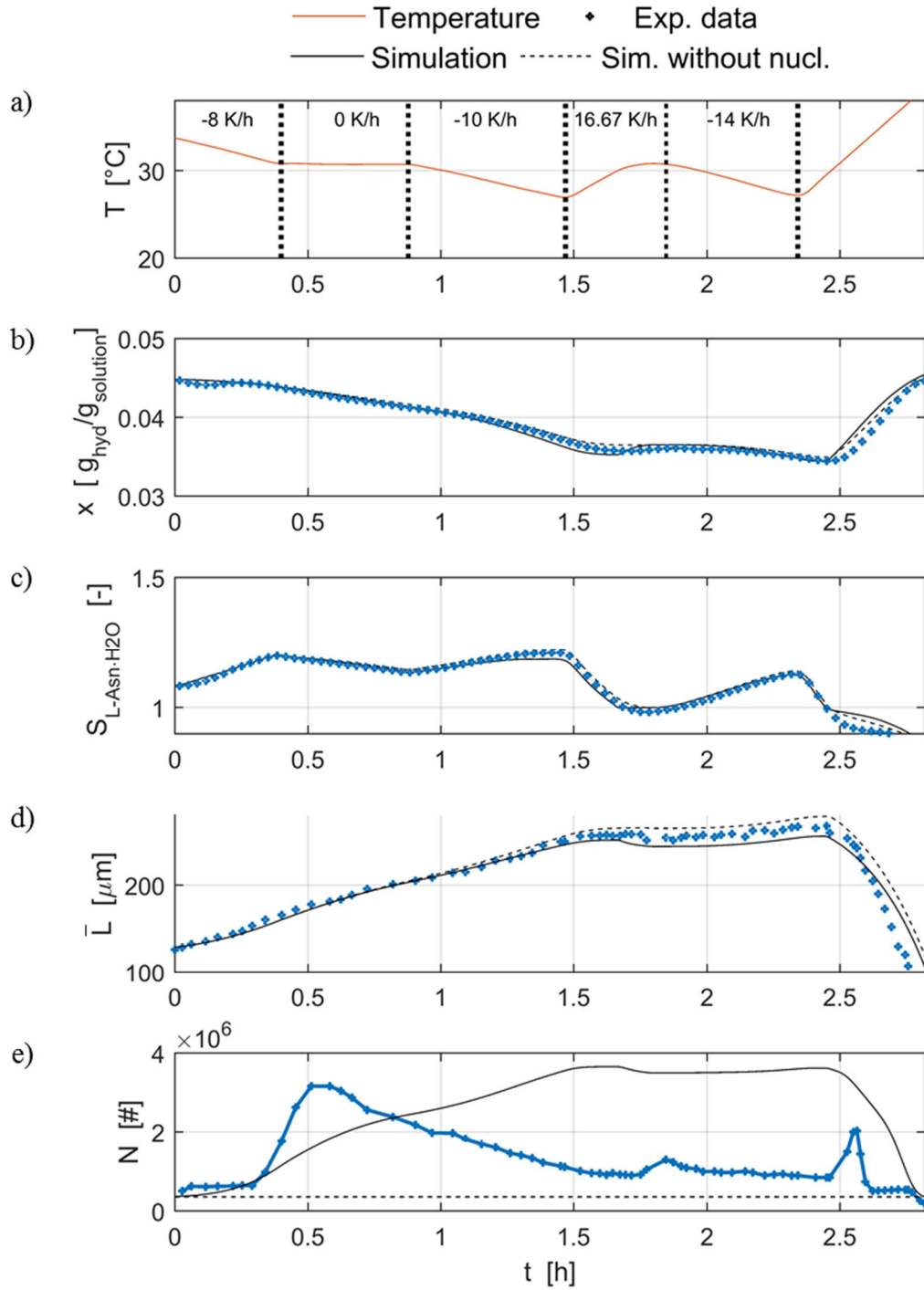


Fig. 18: Measured quantities of the validation experiment Val-L1 in comparison with simulated values utilizing the previously estimated crystallization kinetics from pure L-Asn solutions. a) Temperature profile with indicated cooling and heating rates. b) Concentrations of L-Asn. c) Transient supersaturation. d) Seed crystal mean size evolution. e) Transient single particle

number. Blue dots and curves - L-Asn; Black solid lines - simulation results applying the crystallization kinetics from pure L-Asn solutions; Black dashed lines - simulation results without nucleation.

A major challenge for the estimation of nucleation kinetics is, beside the accuracy and resolution of the measurement technique, growth rate dispersion (GRD). In figure 19, the simulation is compared to the measured transient crystal size distributions of experiment L2. The evolution of the seeded particles agrees well similar to the evaluation experiments but the trend of the nuclei deviates significantly in the simulation (Fig. 19 a).

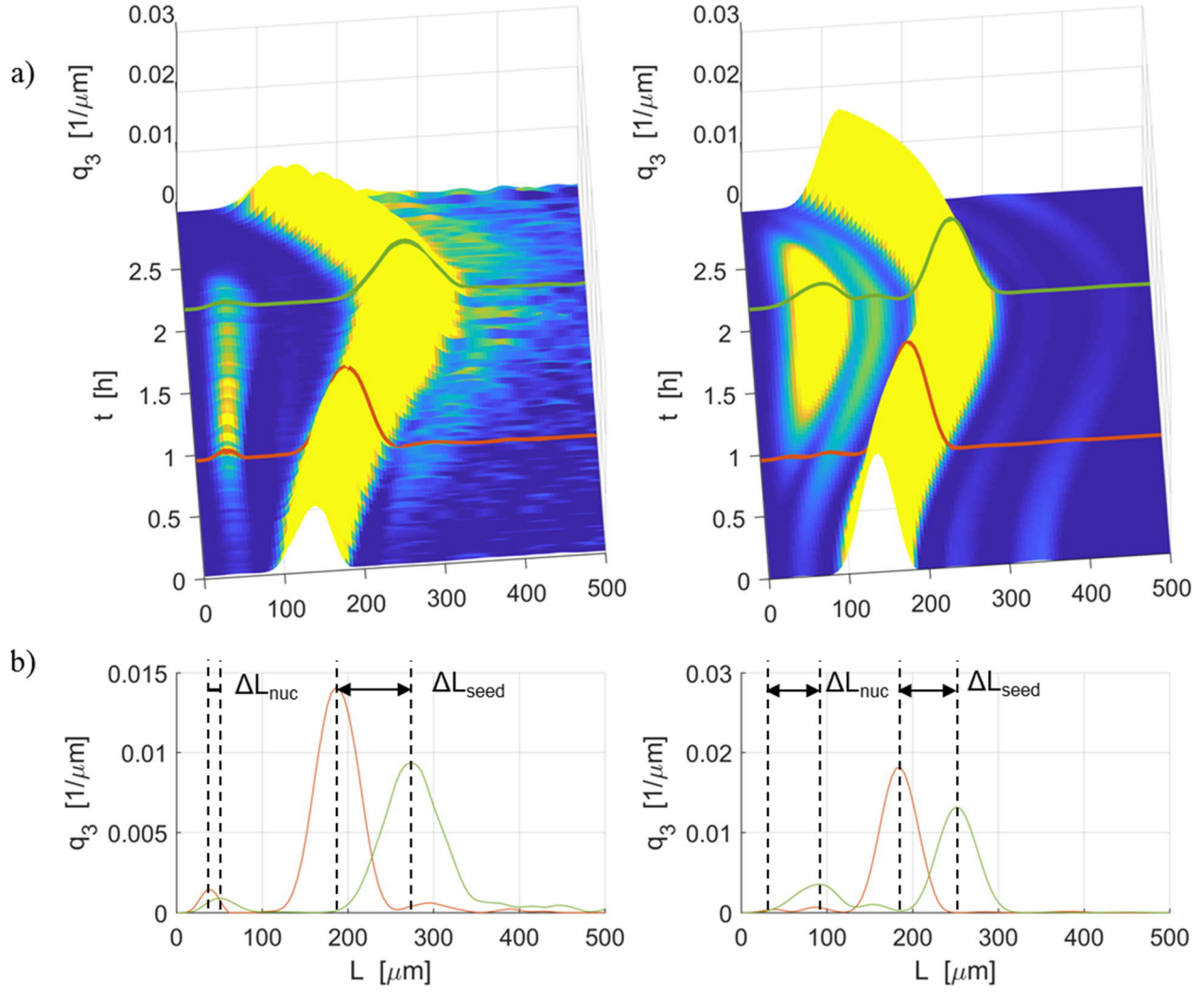


Fig. 19: Measured size distribution of experiment L2 (*left*) in comparison to simulation (*right*).

a) Transient size distributions with two lines indicating snapshots, which are depicted below. b) Comparison of two distributions at 1h and 2.2h showing the significant impact of growth rate dispersion.

The observed change in mean size between the seed crystals (ΔL_{seed} in Fig. 19 b) is drastically larger than the change in size of the smaller particles (ΔL_{nuc} in Fig. 19 b) while in the simulation the same growth rate for all particles is assumed ($\Delta L_{\text{seed}} = \Delta L_{\text{nuc}}$ in Fig. 19 b), *right*). Hence, in experiments, less solute is consumed by growth of the nuclei, which explains partly the

deviations to the model predictions. An appropriate quantification method for growth rate dispersion, especially GRD of nuclei, cannot be reported up to now. It should be a field of further research to improve PBE models.

5. Conclusions

The growth kinetics from racemic asparagine solutions and the nucleation, growth and dissolution kinetics from pure L-Asn solutions were estimated on the basis of a few seeded batch crystallizations. The necessary driving force calculation was discussed in detail on the basis of the phase diagram to explain the observations during a Preferential Crystallization. Furthermore, a description of the solubility surfaces of D-/L-Asn-H₂O with composition and temperature was derived to determine the individual supersaturations during the experiments.

A simple experimental setup consisting of online microscopy, densitometry and offline HPLC analysis was shown to be sufficient to follow the crystal size evolution and liquid phase composition. Altogether, the data of seven experiments was utilized for the parameter estimation procedure to quantify the crystallization kinetics of L-Asn-H₂O seeds in racemic and pure L-Asn solutions.

It was shown, that the growth kinetics is significantly influenced by the counter enantiomers presence. The counter enantiomer acts as an additive altering the kinetics probably due to the structural similarities, which lead to strong interaction at crystal surface. Especially for crystallization-based enantioseparation processes, the dependency of the growth kinetics to the liquid phase compositions has to be considered since it complicates the separation, model-based description and process optimization.

The estimated dissolution kinetics from pure L-Asn solutions were applied for describing both, experiments from racemic and enantiopure solutions. A strong influence on the liquid phase composition was not visible in this case probably due to the high dissolution rates, which made a precise measurement challenging. However, a good agreement was found applying the estimated dissolution parameters for the simulated and measured liquid phase concentration and driving force but small deviations occurred for the description of the solid phase. Also the estimated secondary nucleation kinetics from pure L-Asn solutions was not capable to describe the system behavior completely. A possible reason is growth rate dispersion, which was proven to have a significant influence on the crystal phase. Nevertheless, the overall process trends of asparagine monohydrate crystallization from enantiopure and racemic solutions can be simulated in good quality with the found kinetics as shown on the example of the validation experiments.

List of symbols

B_0	[#/s]	Nucleation rate
D	[m/s]	Dissolution rate
f	[#/m]	Number density distribution/ function
Feret	[μm]	Feret diameter
G	[m/s]	Growth rate
kV	[-]	Volume shape factor
K	[-; $1/^\circ\text{C}$; $1/^\circ\text{C}^2$]	Parameter in (eq. 3)
K	[m/s; 1/s]	Kinetic G , B_0 or D in (eq. 10)
L	[μm ; m]	Property coordinate
\bar{L}	[μm ; m]	Mean length
M	[g/mol]	Molar mass

m	[kg]	Mass
N	[#]	Crystal number
n	[-]	Number
OF	[m; #]	Objective function
p	[-]	Parameters for the kinetic laws
q ₀	[-]	Relative number distribution
q ₃	[-]	Relative mass distribution
R	[J/K·mol]	Universal gas constant
S	[-]	Relative supersaturation
T	[°C]	Temperature
t	[h]	Time
x	[-]	Mass fraction
\dot{V}	[mL/min]	Volumetric flow rate
ρ	[kg/m ³]	Density

Sub- & Superscripts

anhydr.	Anhydrate
B	Nucleation
cryst	Crystallization
D	Dissolution
L(·H ₂ O)	L-enantiomer (monohydrate)
DL	Racemic composition
end	End
Exp	Experiment

G	Growth
H ₂ O	Water
hydr.	Hydrate
i/ j	Component i/ j; count variables
L-Asn·H ₂ O	L-asparagine monohydrate
max	Maximal
meas	Measured
min	Minimal
nuc	Nucleation
sat	Saturation
sec	Secondary
seed	Seed
sim	Simulated
solid	Solid
susp	Suspension
0	Initial value

References

- [1] Randolph, D. R.; Larson, M. A. *Theory of Particulate Processes*, 2nd ed., Academic Press Inc., San Diego, 1988.
- [2] Ramkrishna, D. *Population Balances - Theory and Applications to Particulate Systems in Engineering*, Academic Press Inc., San Diego, 2000.

- [3] Eicke, M. J.; Levilain, G.; Seidel-Morgenstern, A. Efficient Resolution of Enantiomers by Coupling Preferential Crystallization and Dissolution. Part 2. A Parametric Simulation Study To Identify Suitable Process Conditions, *Cryst. Growth Des.* **2013**, 13, pp. 1638-1648. <https://doi.org/10.1021/cg3018503>.
- [4] Köllges, T.; Vetter, T. Model-Based Analysis of Continuous Crystallization/Reaction Processes Separating Conglomerate Forming Enantiomers, *Cryst. Growth Des.* **2017**, 17, pp. 233-247. <https://doi.org/10.1021/acs.cgd.6b01487>.
- [5] Lin, F. B.; Meleshko, S. V.; Flood, A. E. Exact solutions of the population balance equation including particle transport, using group analysis, *Commun. Nonlinear Sci. Numer. Simulat.* **2018**, 59, pp. 255–271. <https://doi.org/10.1016/j.cnsns.2017.11.022>.
- [6] Maggioni, G. M.; Bezing, L.; Mazzotti, M. Stochastic Nucleation of Polymorphs: Experimental Evidence and Mathematical Modeling, *Cryst. Growth Des.* **2017**, 17, pp. 6703-6711. <https://doi.org/10.1021/acs.cgd.7b01313>.
- [7] Mangold, M.; Khlopov, D.; Temmel, E.; Lorenz, H.; Seidel-Morgenstern, A. Modelling geometrical and fluid-dynamic aspects of a continuous fluidized bed crystallizer for separation of enantiomers, *Chem. Eng. Sci.* **2017**, 160, pp. 281-290. <https://doi.org/10.1016/j.ces.2016.11.042>.
- [8] Perez-Calvo, J.; Kadam, S. S.; Kramer, H. J. M. Determination of kinetics in batch cooling crystallization processes: A sequential parameter estimation approach, *AIChE Journal* **2016**, 62, pp. 3992-4012. <https://doi.org/10.1002/aic.15295>.

- [9] Qamar, S.; Galan, K.; Elsner, M. P.; Hussain, I.; Seidel-Morgenstern, A. Theoretical investigation of simultaneous continuous preferential crystallization in a coupled mode, *Chem. Eng. Sci.* **2013**, 98, pp. 25-39. <https://doi.org/10.1016/j.ces.2013.05.010>.
- [10] Salvatori, F.; Mazzotti, M.; Manipulation of Particle Morphology by Crystallization, Milling, and Heating Cycles-A Mathematical Modeling Approach, *Ind. Eng. Chem. Res.* **2017**, 56, pp. 9188-9201. <https://doi.org/10.1021/acs.iecr.7b02070>.
- [11] Briançon, S.; Colson, D.; Klein, J. P. Modelling of crystalline layer growth using kinetic data obtained from suspension crystallization, *Chem. Eng. J.* **1998**, 70, pp. 55-64. [https://doi.org/10.1016/S1385-8947\(98\)00080-1](https://doi.org/10.1016/S1385-8947(98)00080-1).
- [12] Har, C. L.; Fu, N.; Chan, E. S.; Tey, B. T.; Chen, X. D. In situ crystallization kinetics and behavior of mannitol during droplet drying, *Chem. Eng. J.* **2018**, 354, pp. 314-326. <https://doi.org/10.1016/j.cej.2018.07.202>.
- [13] Aldaco, R.; Garea, A.; Irabien, A. Modeling of particle growth: Application to water treatment in a fluidized bed reactor, *Chem. Eng. J.* **2007**, 134, pp. 66-71. <https://doi.org/10.1016/j.cej.2007.03.068>.
- [14] Temmel, E.; Eisenschmidt, H.; Lorenz, H.; Seidel-Morgenstern, A. A Short-Cut Method for the Quantification of Crystallization Kinetics 1. Method Development, *Cryst. Growth Des.* **2016**, 16, pp. 6743-6755. <https://doi.org/10.1021/acs.cgd.6b00787>.
- [15] Temmel, E.; Eicke, M.; Lorenz, H.; Seidel-Morgenstern, A. A Short-Cut Method for the Quantification of Crystallization Kinetics. 2. Experimental Application, *Cryst. Growth Des.*

- 2016**, 16, pp. 6756-6768. <https://doi.org/10.1021/acs.cgd.6b00789>.
- [16] Garside, J.; Mersmann, A.; Nyvlt J. (eds.) *Measurement of Crystal Growth Rates*, European Federation of Chemical Engineering, München, 1990.
- [17] Bhoi, S.; Sarkar, D. Modelling and experimental validation of ultrasound assisted unseeded batch cooling crystallization of L-asparagine monohydrate, *Cryst. Eng. Comm.* **2016**, 18, pp. 4863-4874. <https://doi.org/10.1039/c6ce00937a>.
- [18] Lindenberg, C.; Mazzotti, M. Continuous Precipitation of L-Asparagine Monohydrate in a Micromixer: Estimation of Nucleation and Growth Kinetics, *AIChE Journal* **2011**, 57, pp. 942-950. <https://doi.org/10.1002/aic.12326>.
- [19] Kongsamai, P.; Maneedaeng, A.; Flood, C.; ter Horst, J. H.; Flood, A. E. Effect of additives on the preferential crystallization of L-asparagine monohydrate, *Eur. Phys. J. Spec. Top.* **2017**, 226, pp. 823-835. <https://doi.org/10.1140/epjst/e2016-60257-3>.
- [20] Kongsamai, P.; Flood, C.; ter Horst, J. H.; Flood, A. E.; Particle Size Distributions and Performance of Preferential Crystallization of L-Asparagine center dot H₂O with Tailor-Made Additives, *Chem. Eng. Tech.* **2018**, 41, pp. 1173-1179. <https://doi.org/10.1002/ceat.201700668>.
- [21] Petruševska-Seebach, K. *Overcoming yield limitations when resolving racemates by combination of crystallization and/or chromatography with racemization*, PhD Thesis, docupoint, Barleben, 2012.

- [22] Lorenz, H.; Temmel, E.; Seidel-Morgenstern, A. *Continuous Enantioselective Crystallization of Chiral Compounds*, in: N. Yazdanpanah, Z. Nagy (eds.), *Handbook of Continuous Crystallization*, Royal Society of Chemistry, London, - book in press -.
- [23] Borchert, C.; Sundmacher, K. Crystal Aggregation in a Flow Tube: Image-Based Observation, *Chem. Eng. Tech.* **2011**, 34, pp. 545-556.
<https://doi.org/10.1002/ceat.201000465>.
- [24] Borchert, C.; Temmel, E.; Eisenschmidt, H.; Lorenz, H.; Seidel-Morgenstern, A.; Sundmacher, K. Image-Based in Situ Identification of Face Specific Crystal Growth Rates from Crystal Populations, *Cryst. Growth Des.* **2014**, 14, pp. 952-971.
<https://doi.org/10.1021/cg401098x>.
- [25] Jacques, J.; Collet, A.; Wilen, S. H. *Enantiomers, Racemates and Resolutions*, Krieger, Malabar, 1994.

For Table of Contents Use Only

Title:

Measurement and evaluation of the crystallization kinetics of L-asparagine monohydrate in the ternary L-/ D-asparagine/ water system

Authors:

Erik Temmel, Jonathan Gänsch, Heike Lorenz, Kai Sundmacher, Andreas Seidel-Morgenstern

Synopsis:

Growth kinetics of L-asparagine monohydrate in racemic aqueous solutions as well as nucleation, growth and dissolution kinetics of the same enantiomer crystallized from pure L-asparagine solutions are measured and the kinetic parameters are estimated applying a recently developed shortcut-method. It is proven that growth kinetics of L- and D-asparagine monohydrate from water are identical but, in contrast, that the growth kinetics from racemic and enantiopure solutions of asparagine differ significantly from each other.

TOC graphic

